Analytical bond-order potential for the Cd-Zn-Te ternary system

D. K. Ward,[1] X. W. Zhou,[2] B. M. Wong,[3] F. P. Doty,[1] and J. A. Zimmerman[2]

[1]*Radiation and Nuclear Detection Materials and Analysis Department, Sandia National Laboratories, Livermore, California 94550, USA*

[2]*Mechanics of Materials Department, Sandia National Laboratories, Livermore, California 94550, USA*

[3]*Materials Chemistry Department, Sandia National Laboratories, Livermore, California 94550, USA*

(Received 12 July 2012; published 17 December 2012)

Cd-Zn-Te ternary alloyed semiconductor compounds are key materials in radiation detection and photovoltaic applications. Currently, crystalline defects such as dislocations limit the performance of these materials. Atomistic simulations are a powerful method for exploring crystalline defects at a resolution unattainable by experimental techniques. To enable accurate atomistic simulations of defects in the Cd-Zn-Te systems, we develop a full Cd-Zn-Te ternary bond-order potential. This Cd-Zn-Te potential has numerous unique advantages over other potential formulations: (1) It is analytically derived from quantum mechanical theories and is therefore more likely to be transferable to environments that are not explicitly tested. (2) A variety of elemental and compound configurations (with coordination varying from 1 to 12) including small clusters, bulk lattices, defects, and surfaces are explicitly considered during parameterization. As a result, the potential captures structural and property trends close to those seen in experiments and quantum mechanical calculations and provides a good description of melting temperature, defect characteristics, and surface reconstructions. (3) Most importantly, this potential is validated to correctly predict the crystalline growth of the ground-state structures for Cd, Zn, Te elements as well as CdTe, ZnTe, and $Cd_{1-x}Zn_xTe$ compounds during highly challenging molecular dynamics vapor deposition simulations.

DOI: 10.1103/PhysRevB.86.245203 PACS number(s): 34.20.Cf, 31.15.xv, 71.15.Nc, 81.15.−z

I. INTRODUCTION

$Cd_{1-x}Zn_xTe$ crystals have long been the dominant semiconductor materials for radiation detection.[1–4] Unfortunately, these materials tend to have nonuniform properties, resulting in both limited performance and high material cost (arising from a low yield of usable portions of ingots).[1] The nonuniformity properties have been attributed to such defects as Te particles[5,6] and dislocation networks.[1,7–11] Previous efforts to improve the materials have focused on reducing Te particles, but little work has focused on dislocation network structures. $Cd_{1-x}Zn_xTe$ crystals are also important semiconductor materials for photovoltaic applications. Currently, the cost of CdTe/CdS solar cells has reached \$0.15/kWh, lower than any other photovoltaic technology.[12] However, recent studies[13,14] have indicated that large lattice mismatch between CdTe and CdS results in a very high misfit dislocation density that limits the properties. These results suggest that growing graded $Cd_{1-x}Zn_xTe$ nanoislands on CdS may reduce the misfit dislocation density as these islands both have better lattice match with CdS and allow mismatch strain to be relaxed in three dimensions. Exploring network evolution due to a large number (combinations of shuffle and glide, α and β, partial and perfect, edge, screw, and mixed, etc.) of different types of dislocations and misfit dislocation formation during growth of nanoislands is extremely challenging in experiments. Atomistic simulations offer an alternative method to efficiently study dislocation behavior in $Cd_{1-x}Zn_xTe$ crystals and then guide experiments to improve the materials. Such atomistic simulations require a high fidelity Cd-Zn-Te ternary interatomic potential that can be transferrable to defect regions.

A transferrable interatomic potential should satisfy simultaneously two criteria: It captures property trends of a variety of predefinable clusters, lattices, defects, and surfaces; and it must also correctly predict the crystalline growth of ground-state structures during molecular dynamics growth (e.g. vapor deposition) simulations. The latter criterion is extremely important because it samples a variety of surface configurations not known *a priori*. If the potential overstabilizes an incorrect structure at the surface, the simulation will likely result in amorphous growth. Capturing crystalline growth therefore ensures that a potential is reasonably transferable to all possible configurations. In particular, it offers a strong validation that the potential captures the lowest energy for the ground-state phase. Previous potential development often ignores the critical growth simulation which leads to poorly parameterized functions.[15]

We recently developed a bond-order potential (BOP) for the Cd-Te binary system.[16] This BOP is particularly attractive because it is analytically derived from quantum mechanical theories[17–21] and is therefore more likely to be transferable to environments not explicitly tested. In particular, we demonstrated[16] that our Cd-Te BOP captures the property (i.e., atomic energies, atomic volumes, elastic constants, and melting temperatures) trends of a variety of structures, including clusters, bulk lattices, point defects, and surfaces, and can predict crystalline growth of both elements and compounds during molecular dynamics (MD) vapor deposition simulations. The potential has also been used to capture crystalline melt growth.[22] (Note that we have developed two versions of CdZnTe BOPs. The version discussed here is extended from the published CdTe BOP.[16] These versions of CdTe and CdZnTe BOPs do not capture accurately the experimental lattice constant for zinc-blende CdTe. The other version of CdZnTe BOP captures accurately the lattice constant. While the other version will be published later, both versions are available in the LAMMPS release.)

No ternary BOP has ever been demonstrated. This paper looks to develop a ternary high-fidelity Cd-Zn-Te BOP. In addition to retaining the fidelity of the Cd-Te binary BOP, we require that our Cd-Zn-Te BOP additionally captures

property trends of a large number of Zn, Cd-Zn, Zn-Te, and Cd-Zn-Te clusters and lattices as compared with available experiments and density functional theory (DFT) data. Most critically, we validate that this Cd-Zn-Te BOP correctly predicts the crystalline growth of Zn element as well as ZnTe and $Cd_{1-x}Zn_xTe$ compounds during MD vapor deposition simulations and also correctly predicts the experimentally observed phase separation of the $Cd_{0.5}Zn_{0.5}$ alloy. Equally as important, we demonstrate that the BOP parameterization approach is general and can be used to add more elements in the future. This will enable the advanced BOP approach to address systems with increased complexity.

II. BOP EXPRESSIONS

Physics of the BOP have been discussed in detail previously[16] and hence will not be repeated here. For discussion of BOP parameterization, however, the mathematic formulation of the BOP is listed. In the framework of the BOP,[16] the total energy of a system containing N atoms ($i = 1, 2, \ldots, N$) is expressed as

$$E = \frac{1}{2}\sum_{i=1}^{N}\sum_{j=i_1}^{i_N}\phi_{ij}(r_{ij}) - \sum_{i=1}^{N}\sum_{j=i_1}^{i_N}\beta_{\sigma,ij}(r_{ij})\cdot\Theta_{\sigma,ij} - \sum_{i=1}^{N}\sum_{j=i_1}^{i_N}\beta_{\pi,ij}(r_{ij})\cdot\Theta_{\pi,ij}, \quad (1)$$

where $\phi_{ij}(r_{ij})$, $\beta_{\sigma,ij}(r_{ij})$, and $\beta_{\pi,ij}(r_{ij})$ are pair functions, and $\Theta_{\sigma,ij}$ and $\Theta_{\pi,ij}$ are many-body functions corresponding, respectively, to σ and π bond orders, and the list $j = i_1, i_2, \ldots, i_N$ represents neighbors of atom i. Here, $\phi_{ij}(r_{ij})$, $\beta_{\sigma,ij}(r_{ij})$, and $\beta_{\pi,ij}(r_{ij})$ are expressed in a general form as

$$\phi_{ij}(r_{ij}) = \phi_{0,ij}\cdot f_{ij}(r_{ij})^{m_{ij}}\cdot f_{c,ij}(r_{ij}), \quad (2)$$

$$\beta_{\sigma,ij}(r_{ij}) = \beta_{\sigma,0,ij}\cdot f_{ij}(r_{ij})^{n_{ij}}\cdot f_{c,ij}(r_{ij}), \quad (3)$$

$$\beta_{\pi,ij}(r_{ij}) = \beta_{\pi,0,ij}\cdot f_{ij}(r_{ij})^{n_{ij}}\cdot f_{c,ij}(r_{ij}), \quad (4)$$

where $\phi_{0,ij}$, $\beta_{\sigma,0,ij}$, $\beta_{\pi,0,ij}$, m_{ij}, and n_{ij} are pair (ij) dependent parameters, $f_{ij}(r_{ij})$ is a Goodwin–Skinner–Pettifor (GSP) radial function,[23] and $f_{c,ij}(r_{ij})$ is a cutoff function. The GSP and the cutoff functions are written, respectively, as

$$f_{ij}(r_{ij}) = \frac{r_{0,ij}}{r_{ij}}\exp\left[\left(\frac{r_{0,ij}}{r_{c,ij}}\right)^{n_{c,ij}} - \left(\frac{r_{ij}}{r_{c,ij}}\right)^{n_{c,ij}}\right] \quad (5)$$

and

$$f_{c,ij}(r_{ij}) = \begin{cases} \frac{\exp\left(-\alpha_{ij}\cdot r_{ij}^{\gamma_{ij}}\right)-\exp\left(-\alpha_{ij}\cdot r_{\mathrm{cut},ij}^{\gamma_{ij}}\right)}{\exp\left(-\alpha_{ij}\cdot r_{1,ij}^{\gamma_{ij}}\right)-\exp\left(-\alpha_{ij}\cdot r_{\mathrm{cut},ij}^{\gamma_{ij}}\right)}, & r_{ij} < r_{\mathrm{cut},ij} \\ 0, & r_{ij} \geqslant r_{\mathrm{cut},ij} \end{cases}, \quad (6)$$

where $r_{0,ij}$, $r_{c,ij}$, $n_{c,ij}$, $r_{1,ij}$, and $r_{\mathrm{cut},ij}$ are independent pair parameters (in particular, $r_{\mathrm{cut},ij}$ represents the cutoff distance of the potential), and γ_{ij} and α_{ij} are dependent pair parameters defined as

$$\gamma_{ij} = \frac{\ln[\ln(0.99)/\ln(0.01)]}{\ln(r_{1,ij}/r_{\mathrm{cut},ij})} \quad \text{and} \quad \alpha_{ij} = -\frac{\ln(0.99)}{(r_{1,ij})^{\gamma_{ij}}}.$$

The σ bond order $\Theta_{\sigma,ij}$ used in Eq. (1) is calculated as

$$\Theta_{\sigma,ij} = \Theta_{s,ij}\left(\Theta_{\sigma,ij}^{(1/2)}, f_{\sigma,ij}\right)\left[1 - \left(f_{\sigma,ij} - \frac{1}{2}\right)\cdot k_{\sigma,ij}\cdot\frac{\beta_{\sigma,ij}^2(r_{ij})\cdot R_{3\sigma,ij}}{\beta_{\sigma,ij}^2(r_{ij}) + \frac{\beta_{\sigma,ij}^2(r_{ij})\cdot\Phi_{2\sigma}^i + \beta_{\sigma,ij}^2(r_{ij})\cdot\Phi_{2\sigma}^j}{2} + \varsigma_2}\right], \quad (7)$$

where $0 \leqslant f_{\sigma,ij} \leqslant 1$ and $k_{\sigma,ij}$ are, respectively, band filling and skewing pair parameters, $\Phi_{2\sigma}^i$, $\Phi_{2\sigma}^j$, and $R_{3\sigma,ij}$ are local variables that can be calculated from atom positions, ς_2 is a constant, and $\Theta_{s,ij}$ is a symmetric band-filling function that modifies the half-full valence shell bond-order expression $\Theta_{\sigma,ij}^{(1/2)}$. Here, $\Theta_{s,ij}$ as a function of $\Theta_{\sigma,ij}^{(1/2)}$ can be well described by

$$\Theta_{s,ij}\left[\Theta_{\sigma,ij}^{(1/2)}\right] = \frac{\Theta_0 + \Theta_1 + S\cdot\Theta_{\sigma,ij}^{(1/2)} - \sqrt{\left[\Theta_0 + \Theta_1 + S\cdot\Theta_{\sigma,ij}^{(1/2)}\right]^2 - 4\left[-\varepsilon\sqrt{1+S^2} + \Theta_0\cdot\Theta_1 + S\cdot\Theta_1\cdot\Theta_{\sigma,ij}^{(1/2)}\right]}}{2}, \quad (8)$$

where

$$\begin{aligned} \varepsilon &= 10^{-10} \\ \Theta_0 &= 15.737980\cdot\left(\tfrac{1}{2} - \left|f_{\sigma,ij} - \tfrac{1}{2}\right|\right)^{1.137622}\cdot\left|f_{\sigma,ij} - \tfrac{1}{2}\right|^{2.087779} \\ S &= 1.033201\cdot\left\{1 - \exp\left[-22.180680\cdot\left(\tfrac{1}{2} - \left|f_{\sigma,ij} - \tfrac{1}{2}\right|\right)^{2.689731}\right]\right\} \\ \Theta_1 &= 2\cdot\left(\tfrac{1}{2} - \left|f_{\sigma,ij} - \tfrac{1}{2}\right|\right). \end{aligned} \quad (9)$$

To use Eq. (7), expressions of the half-full bond order $\Theta_{\sigma,ij}^{(1/2)}$ and local variables $\Phi_{2\sigma}^i$, $\Phi_{2\sigma}^j$, $R_{3\sigma,ij}$ are further needed. Here, $\Theta_{\sigma,ij}^{(1/2)}$ is expressed as

$$\Theta_{\sigma,ij}^{(1/2)} = \frac{\beta_{\sigma,ij}(r_{ij})}{\sqrt{\beta_{\sigma,ij}^2(r_{ij}) + c_{\sigma,ij}\cdot\left[\beta_{\sigma,ij}^2(r_{ij})\cdot\Phi_{2\sigma}^i + \beta_{\sigma,ij}^2(r_{ij})\cdot\Phi_{2\sigma}^j\right] + \varsigma_1}}, \quad (10)$$

where $c_{\sigma,ij}$ is a pair parameter and ς_1 is a constant. The $\Phi^i_{2\sigma}$ and $\Phi^j_{2\sigma}$ terms have the same formulation except that they are evaluated at the center of atom i and atom j, respectively. Considering that Eqs. (7) and (10) use only the product $\beta^2_{\sigma,ij}(r_{ij})\cdot\Phi^i_{2\sigma}$, we only give the formula for $\beta^2_{\sigma,ij}(r_{ij})\cdot\Phi^i_{2\sigma}$ as

$$\beta^2_{\sigma,ij}(r_{ij})\cdot\Phi^i_{2\sigma} = \sum_{\substack{k=i_1\\k\neq j}}^{i_N} g^2_{\sigma,jik}(\theta_{jik})\cdot\beta^2_{\sigma,ik}(r_{ik}), \tag{11}$$

where θ_{jik} is the bond angle at atom i spanning atoms j and k, and the three-body angular function $g_{\sigma,jik}(\theta_{jik})$ is written as

$$g_{\sigma,jik}(\theta_{jik}) = \frac{(b_{\sigma,jik}-g_{0,jik})\cdot u^2_{\sigma,jik}-(g_{0,jik}+b_{\sigma,jik})\cdot u_{\sigma,jik}}{2\cdot\left(1-u^2_{\sigma,jik}\right)} + \frac{g_{0,jik}+b_{\sigma,jik}}{2}\cos\theta_{jik}$$
$$+\frac{g_{0,jik}-b_{\sigma,jik}+(g_{0,jik}+b_{\sigma,jik})\cdot u_{\sigma,jik}}{2\cdot\left(1-u^2_{\sigma,jik}\right)}\cdot\cos^2\theta_{jik}, \tag{12}$$

where $g_{0,jik}$, $b_{\sigma,jik}$, and $u_{\sigma,jik}$ are three-body-dependent parameters.

Similarly, we give the product of $\beta^2_{\sigma,ij}(r_{ij})\cdot R_{3\sigma,ij}$ as

$$\beta^2_{\sigma,ij}(r_{ij})\cdot R_{3\sigma,ij} = \sum_{\substack{k=i_1\\k,j=n}}^{i_N} g_\sigma(\theta_{jik})\cdot g_\sigma(\theta_{ijk})\cdot g_\sigma(\theta_{ikj})\cdot\beta_{\sigma,ik}(r_{ik})\cdot\beta_{\sigma,jk}(r_{jk}), \tag{13}$$

where $k,j=n$ in the summation indicates that k and j are neighbors.

The π bond-order $\Theta_{\pi,ij}$ used in Eq. (1) is expressed as

$$\Theta_{\pi,ij} = \frac{a_{\pi,ij}\cdot\beta_{\pi,ij}(r_{ij})}{\sqrt{\beta^2_{\pi,ij}(r_{ij})+c_{\pi,ij}\cdot\left(\frac{\beta^2_{\pi,ij}(r_{ij})\cdot\Phi^i_{2\pi}+\beta^2_{\pi,ij}(r_{ij})\cdot\Phi^j_{2\pi}}{2}+\sqrt{\beta^4_{\pi,ij}(r_{ij})\cdot\Phi_{4\pi}+\varsigma_3}\right)+\varsigma_4}}$$
$$+\frac{a_{\pi,ij}\cdot\beta_{\pi,ij}(r_{ij})}{\sqrt{\beta^2_{\pi,ij}(r_{ij})+c_{\pi,ij}\cdot\left(\frac{\beta^2_{\pi,ij}(r_{ij})\cdot\Phi^i_{2\pi}+\beta^2_{\pi,ij}(r_{ij})\cdot\Phi^j_{2\pi}}{2}-\sqrt{\beta^4_{\pi,ij}(r_{ij})\cdot\Phi_{4\pi}+\varsigma_3}+\sqrt{\varsigma_3}\right)+\varsigma_4}}, \tag{14}$$

where $a_{\pi,ij}$ and $c_{\pi,ij}$ are pair parameters, ς_3 and ς_4 are constants, and $\Phi^i_{2\pi}$, $\Phi^j_{2\pi}$, $\Phi_{4\pi}$ are local variables. For calculations using Eq. (14), the $\beta^2_{\pi,ij}(r_{ij})\cdot\Phi^i_{2\pi}$ and $\beta^4_{\pi,ij}(r_{ij})\cdot\Phi_{4\pi}$ terms are further expressed as

$$\beta^2_{\pi,ij}(r_{ij})\cdot\Phi^i_{2\pi} = \sum_{\substack{k=i_1\\k\neq j}}^{i_N}\left[p_{\pi,i}\cdot\beta^2_{\sigma,ik}(r_{ik})\cdot\sin^2\theta_{jik}+(1+\cos^2\theta_{jik})\cdot\beta^2_{\pi,ik}(r_{ik})\right], \tag{15}$$

$$\beta^4_{\pi,ij}(r_{ij})\cdot\Phi_{4\pi} = \frac{1}{4}\sum_{\substack{k=i_1\\k\neq j}}^{i_N}\sin^4\theta_{jik}\cdot\hat\beta^4_{ik}(r_{ik})+\frac{1}{4}\sum_{\substack{k=j_1\\k\neq i}}^{j_N}\sin^4\theta_{ijk}\cdot\hat\beta^4_{jk}(r_{jk})$$
$$+\frac{1}{2}\sum_{\substack{k=i_1\\k\neq j}}^{i_N}\sum_{\substack{k'=k+1\\k'\neq j}}^{i_N}\sin^2\theta_{jik}\cdot\sin^2\theta_{jik'}\cdot\hat\beta^2_{ik}(r_{ik})\cdot\hat\beta^2_{ik'}(r_{ik'})\cdot\cos(\Delta\psi_{kk'})$$
$$+\frac{1}{2}\sum_{\substack{k=j_1\\k\neq i}}^{j_N}\sum_{\substack{k'=k+1\\k'\neq i}}^{j_N}\sin^2\theta_{ijk}\cdot\sin^2\theta_{ijk'}\cdot\hat\beta^2_{jk}(r_{jk})\cdot\hat\beta^2_{jk'}(r_{jk'})\cdot\cos(\Delta\psi_{kk'})$$
$$+\frac{1}{2}\sum_{\substack{k'=i_1\\k'\neq j}}^{i_N}\sum_{\substack{k=j_1\\k\neq i}}^{j_N}\sin^2\theta_{jik'}\cdot\sin^2\theta_{ijk}\cdot\hat\beta^2_{ik'}(r_{ik'})\cdot\hat\beta^2_{jk}(r_{jk})\cdot\cos(\Delta\psi_{kk'}), \tag{16}$$

where

$$\hat\beta^2_{ik}(r_{ik}) = p_{\pi,i}\cdot\beta^2_{\sigma,ik}(r_{ik})-\beta^2_{\pi,ik}(r_{ik}), \tag{17}$$

$p_{\pi,i}$ is a species-dependent parameter of the central atom i, and $\Delta\psi_{kk'}$ is a four-body dihedral angle. The dihedral angular terms can be calculated using the relation

$$\cos(\Delta\psi_{kk'}) = \begin{cases} \frac{2\left(\cos\theta_{kik'} - \cos\theta_{jik'}\cdot\cos\theta_{jik}\right)^2}{\sin^2\theta_{jik}\cdot\sin^2\theta_{jik'}} - 1 & \text{for } k \text{ and } k' \text{ neighors of } i \text{ or,} \\ \frac{2\left(\frac{\vec{ik'}\cdot\vec{jk}}{|\vec{ik'}|\cdot|\vec{jk}|} + \cos\theta_{ijk}\cdot\cos\theta_{jik'}\right)^2}{\sin^2\theta_{ijk}\cdot\sin^2\theta_{jik'}} - 1 & \text{for } k' \text{ neighbor of } i \text{ and } k \text{ neighbor of } j. \end{cases} \quad (18)$$

III. PARAMETERIZATION

As the previous work[16] has shown, parameterization of BOP can be done independently for each interaction type. For instance, the Cd-Zn-Te system can be parameterized first for the elemental Cd, Te, and Zn, then for the binary Cd-Te, Cd-Zn, and Zn-Te, and finally for the ternary Cd-Zn-Te. This important aspect allows new elements to be added without affecting the parameters determined for the previous systems. Our previous work has already parameterized the elemental Cd and Te, as well as the binary Cd-Te.[16] Here, we will progressively parameterize Zn, Cd-Zn, Zn-Te, and Cd-Zn-Te.

Parameterizing BOP or Tersoff potentials for accurate growth simulations is not difficult if a careful and sufficient scheme is implemented. As has been established,[16] the key to parameterizing such a potential is to (1) include a large set of carefully selected target structures and their weight factors in the fitting; (2) impose the correct bounds for the parameters; (3) apply a two-step algorithm with the key pair parameters first determined by fitting to the nearest neighbor structures and the remaining parameters fitted to more complex structures; (4) fully optimize the fitting function; and (5) iteratively add or remove structures and modify their weight factors according to vapor deposition simulation test results.

A complete set of BOP parameters for the Cd-Zn-Te system is listed in Tables I–III. The Cd-Te parameters are taken directly from the previous work,[16] including $\zeta_1 - \zeta_4$ of Table I. The unknown BOP parameters include one point-dependent parameter p_π for the new element Zn; 10 GSP pair parameters r_0, r_c, r_1, r_{cut}, n_c, m, n, ϕ_0, $\beta_{\sigma,0}$, and $\beta_{\pi,0}$ and five additional pair parameters c_σ, f_σ, k_σ, c_π, and a_π for each of the three new pairs ZnZn, CdZn, ZnTe; and three three-body-dependent parameters g_0, b_σ, and u_σ for each of the 12 new three-bodies CdCdZn, TeCdZn, ZnCdZn, CdTeZn, TeTeZn, ZnTeZn, CdZnCd, CdZnTe, CdZnZn, TeZnTe, TeZnZn, and ZnZnZn. Thus, there are a total of $1 \times 1 + 15 \times 3 + 3 \times 12 = 82$ parameters to be determined. However, many parameters can be determined prior to the fitting process. In particular, the characteristic bond lengths r_0, r_c, r_1, and r_{cut} are selected as shown in Table II based upon the criteria that r_0 approximately scales with the bond length of the corresponding atomic pair in the equilibrium structure, r_c equals r_0, r_{cut} roughly scales with r_0, and r_1 is midway between r_0 and r_{cut}. The pair parameters c_π and a_π are set to unity as were originally derived for the π bond order.[18,19] The ZnTe zb crystal structure has a half-full valence shell and does not make use of the symmetric and asymmetric σ bond-order terms; therefore, we set $f_\sigma = 0.50$ and $k_\sigma = 0$ for the Zn-Te bonds. Finally, we set the three-body parameter g_σ to be the normalized value of unity for all the triples as shown in Table III. This leaves 50 parameters to be determined.

Using vapor deposition guided tests, we selected a set of target clusters and lattices as shown in the following: For clusters, we have dimer (di), trimer (tri), square (sq), rhombus (rhom), tetrahedron (tetra), and four-atom-chain (ch) for each of the four materials (element or compound) Zn, Te, ZnTe, CdZn, plus four nonstoichiometric trimers Cd_2Zn, $CdZn_2$, Zn_2Te, and $ZnTe_2$. (Here, nonstoichiometric only means that the ratio for the two species in the binary compound does not equal 1:1.) For lattices, we have diamond-cubic (dc), simple-cubic (sc), body-centered-cubic (bcc), face-centered-cubic (fcc), hexagonal-close-packed (hcp), and graphite (gra) phases for Zn and the same for Te with the addition of γ-Se (A8); zinc-blende (zb), wurtzite (wz), NaCl (B1), CsCl (B2), binary-graphite (bgra), binary-graphene (bgrap), AuCu ($L1_0$), CuPt ($L1_1$), NiAs ($B8_1$), CrB (B33), AlSb (sc16), and face-centered-square (fcs) for the stoichiometric compounds CdZn and ZnTe; Ag_2O (cP4) and ZrO_2 for the four nonstoichiometric compounds Cd_2Zn, $CdZn_2$, Zn_2Te, and $ZnTe_2$; hcp for the $Cd_{0.5}Zn_{0.5}$ alloy; and zb for three ternary alloyed compounds Cd_3ZnTe_4, $CdZnTe_2$, and $CdZn_3Te_4$. Ensuring the lowest energy for the equilibrium phases critically requires incorporating all of these structures. For example, the AuCu ($L1_0$), CuPt ($L1_1$), and AlSb (sc16) structures of the ZnTe compound sometimes became more stable than the equilibrium zinc-blende phase with relatively small changes in the parameters.

Constraining the parameters within physical ranges denotes another important part of the parameterization. Table IV in Appendix A lists these constraints in four groups representing parameterizations of Zn, CdZn, ZnTe, and CdZnTe, respectively.

Previous work[16] has proven that for the nearest neighbor structures (i.e. di, tri, tetra, dc, sc, fcc, gra, zb, wz, NaCl, etc.) whose second nearest neighbor distance is beyond cutoff

TABLE I. Global and point-dependent BOP parameters.

Symbol	ζ_1	ζ_2	ζ_3	ζ_4	$p_{\pi,\text{Cd}}$	$p_{\pi,\text{Te}}$	$p_{\pi,\text{Zn}}$
Value	0.00001	0.00001	0.00100	0.00001	0.420000	0.460686	0.420000

TABLE II. Pair-dependent BOP parameters.

Symbol	CdCd	TeTe	CdTe	ZnZn	CdZn	ZnTe
r_0	3.1276	3.1626	3.1276	2.8220	3.0445	2.6260
r_c	3.1276	3.1626	3.1276	2.8220	3.0445	2.6260
r_1	3.7303	3.8046	4.0138	3.3610	3.5973	3.4976
r_{cut}	4.3330	4.4465	4.9000	3.9000	4.1500	4.3691
n_c	2.800000	2.799998	2.811251	2.800000	2.800000	2.800000
m	3.263155	2.458846	2.587831	2.391751	3.266596	2.129658
n	1.553883	1.223306	1.287478	1.189926	1.641506	1.059531
ϕ_0	0.186369	0.876912	0.631440	0.239479	0.062500	1.162383
$\beta_{\sigma,0}$	0.238318	0.782635	0.825290	0.289444	0.265949	1.174627
$\beta_{\pi,0}$	0.097599	0.531205	0.031743	0.068260	0.003479	0.079133
c_σ	0.561130	1.014809	1.286955	0.124372	3.650000	1.175904
f_σ	0.431863	0.331227	0.500000	0.556696	0.260532	0.500000
k_σ	15.000000	−2.860190	0	−3.878406	11.067344	0
c_π	1	1	1	1	1	1
a_π	1	1	1	1	1	1

distance of the potential), the following three relations hold:

$$E_{b,ij}(r_{ij,0}) = \phi_{ij}(r_{ij,0}) - \beta_{\sigma,ij}(r_{ij,0}) \cdot \frac{\phi'_{ij}(r_{ij,0})}{\beta'_{\sigma,ij}(r_{ij,0})}, \quad (19)$$

$$E''_{b,ij}(r_{ij,0}) = \phi''_{ij}(r_{ij,0}) - \beta''_{\sigma,ij}(r_{ij,0}) \cdot \frac{\phi'_{ij}(r_{ij,0})}{\beta'_{\sigma,ij}(r_{ij,0})}, \quad (20)$$

$$2 \cdot \beta_{\sigma,0,ij} \cdot \Theta_{\sigma,ij} + 2 \cdot \beta_{\pi,0,ij} \cdot \Theta_{\pi,ij} = \beta_{\sigma,0,ij} \cdot \frac{\phi'_{ij}(r_{ij,0})}{\beta'_{\sigma,ij}(r_{ij,0})}, \quad (21)$$

where $E_{b,ij}$ and $E''_{b,ij}$ are the equilibrium energy and the second derivative of the equilibrium energy, respectively, of the nearest neighbor bond at the equilibrium bond length $r_{ij,0}$, $\Theta_{\sigma,ij}$ and $\Theta_{\pi,ij}$ are the equilibrium σ and π bond orders, and subscript ij indicates the species of the pair. The first step of a two-step parameterization determines the pairwise GSP parameters ϕ_0, m, n, and n_c by fitting Eqs. (19) and (20) to the target values (experimental or DFT data) of bond energies (can be converted from cohesive energies) and second derivatives of bond energies (can be converted from bulk moduli) of a wide range of nearest neighbor structures with different equilibrium bond lengths. In particular, optimization is done to minimize the sum of square deviation of Eqs. (19) and (20) from the target values of $E_{b,ij}$ and $E''_{b,ij}$ for a variety of nearest neighbor structures. The parameters determined in the first step enable evaluating the right-hand side of Eq. (21) at the target equilibrium bond lengths for different nearest neighbor structures. This creates a new set of target values for the combined bond-order term $2 \cdot \beta_{\sigma,0,ij} \cdot \Theta_{\sigma,ij} + 2 \cdot \beta_{\pi,0,ij} \cdot \Theta_{\pi,ij}$. These new target values, along with target properties (cohesive energies, lattice constants, etc.) of nonnearest neighbor structures, can then be fitted in a second step to determine the remaining parameters, p_π, $\beta_{\sigma,0}$, $\beta_{\pi,0}$, c_σ, f_σ, k_σ, b_σ, and u_σ. Here, the optimization is done to minimize the sum of square deviation of $2 \cdot \beta_{\sigma,0,ij} \cdot \Theta_{\sigma,ij} + 2 \cdot \beta_{\pi,0,ij} \cdot \Theta_{\pi,ij}$ from the target values for the nearest neighbor structures, plus the sum of square deviation of cohesive

TABLE III. Three-body-dependent BOP parameters.

	Cd-centered triples j−Cd-k					
Symbol	CdCdCd	CdCdTe	CdCdZn	TeCdTe	TeCdZn	ZnCdZn
g_0	1	1	1	1	1	1
b_σ	0.762039	1.000000	0.433692	0.200000	0.882784	0.455028
u_σ	−0.400000	0.099711	0.100000	−0.383360	0.100000	−0.085972
	Te-centered triples j-Te-k					
	CdTeCd	CdTeTe	CdTeZn	TeTeTe	TeTeZn	ZnTeZn
g_0	1	1	1	1	1	1
b_σ	0.200000	0.999854	0.364627	0.669623	0.734966	0.200000
u_σ	−0.400000	−0.003929	−0.333333	−0.141521	0.100000	−0.400000
	Zn-centered triples j-Zn-k					
	CdZnCd	CdZnTe	CdZnZn	TeZnTe	TeZnZn	ZnZnZn
g_0	1	1	1	1	1	1
b_σ	0.200000	0.939572	0.758047	0.200000	1.000000	1.000000
u_σ	−0.223201	−0.400000	0.100000	−0.400000	−0.001972	−0.400000

energies (or other properties) from the target values, and the sum of square deviation of derivatives of cohesive energy with respect to lattice constants from the target value of zero (to fit the lattice constants), for all nonnearest neighbor structures. The fitting procedure gives a weight to each structure with values ranging from 0.5–10. The low energy structures, as determined from DFT, have higher weights.

The potential is optimized using a series of computational tools[24–28] as detailed previously.[16] Following each fitting iteration, the parameters are tested for a larger collection of structures and vapor deposition simulations. If spurious results exist (for example, a structure has a lower cohesive energy than the ground-state phase, or vapor deposition simulations predict an amorphous growth of the equilibrium phase), the entire process is repeated with an appropriate adjustment of target structures and target properties. The iterations continue until a satisfactory set of potential parameters is obtained. Tables I–III list a complete set of BOP parameters thus determined for the Cd-Zn-Te system including global/point-dependent, pair-dependent, and three-body-dependent parameters, respectively.

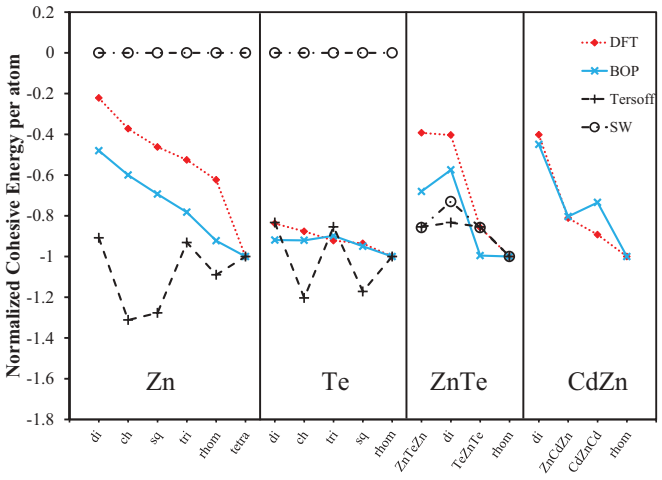

FIG. 1. (Color online) Normalized cohesive energies per atom for selected Zn, Te, ZnTe, and CdZn clusters. Clusters include dimer (di), chain (ch), square (sq), trimer (tri), rhombus (rhom), tetrahedron (tetra).

IV. EVALUATION OF THE POTENTIAL

Previous atomistic simulations of semiconductors have primarily used Stillinger–Weber (SW)[29] and Tersoff[30] potentials. Stillinger–Weber potentials can be easily parameterized to ensure the lowest energy for the ground-state tetrahedral structure (e.g. diamond-cubic and zinc-blende) and its crystalline growth during vapor deposition simulations. However, they cannot capture property trends of different phases.[15] Tersoff potentials fundamentally incorporate the property trends of different phases and can also predict crystalline growth during vapor deposition simulations.[31,32] However, Tersoff potentials are difficult to parameterize to ensure the lowest energy for the ground-state phase and its crystalline growth during vapor deposition simulations. Without involving iterative vapor deposition tests in parameterization, literature Tersoff potentials often incorrectly predict amorphous growth.[15,33,34] The Cd-Zn-Te BOP developed here retains the fidelity of the Cd-Te binary BOP,[16] which broadly improves over the literature SW[35,36] and Tersoff[33] types of Cd-Te potentials. It also represents the development of BOP in a ternary system. Using parallel MD code LAMMPS,[37,38] extensive simulations are performed to evaluate and validate the ternary BOP of structures relevant to Zn and Zn compounds. In particular, geometries and energies of numerous small clusters; lattice constants and cohesive energies of a variety of lattice structures; elastic constants, melting temperature, properties of common point defects (interstitials, vacancies, and antisites), and surface reconstructions of the lowest energy zinc-blende ZnTe compound; and heat of mixing of $Cd_{0.5}Zn_{0.5}$ alloy and $Cd_{1-x}Zn_xTe$ alloyed compounds are all studied. The results obtained from the BOP are compared with those obtained from our high-level DFT calculations, literature (modified) SW[39] and Tersoff[40] potentials for Zn-Te, and published experiments.[41–47] Finally, vapor deposition of Zn, $Cd_{1-x}Zn_x$, ZnTe, and $Cd_{1-x}Zn_xTe$ are simulated.

A. Small-cluster properties

To test BOP's transferability to different environments, the BOP is used in molecular statics energy minimization simulations to calculate relaxed bonding energies and geometries of a variety of Zn, Te, ZnTe, and CdZn clusters with different coordination numbers. The calculated cohesive energies are compared with our corresponding DFT data and the available SW[39] and Tersoff[40] potentials in Fig. 1. Considering that Cd-Te BOP has been evaluated previously,[16] we would need to study only Zn, ZnTe, and CdZn structures. However, Te structures are also included here for a complete comparison with the literature Zn-Te potentials. It should be noted that, while the DFT method captures property trends well, it does not necessarily reproduce the absolute values of the properties measured from experiments. In addition, relative energies determine which structures form during dynamic processes. To better examine the energy trends, we normalize the energies by the magnitudes of the lowest-energy clusters as determined from DFT calculations (tetra for Zn, rhom for Te, ZnTe, and CdZn). We point out that this type of normalization is only used in figures to facilitate the comparison. We will also provide numerically unnormalized data in tables as will be discussed below. Figure 1 shows that BOP does an excellent job reproducing the DFT trends from the low- (large magnitude) to high-energy clusters for Zn, namely tetra → rhom → tri → sq → ch → di, and for Te, rhom → sq → tri → ch → di. Except for a slightly overestimated magnitude (more negative) of the energy for the ZnTeZn trimer and a slightly underestimated magnitude (less negative) of the energy for the CdZnCd trimer, the BOP also gives good energy trends for ZnTe as rhom → TeZnTe → di and for CdZn as rhom → ZnCdZn → di. In comparison to the literature potentials, BOP clearly improves over both the SW and the Tersoff clusters. In particular, the SW potential only assumes repulsive interactions for Zn-Zn and Te-Te pairs[39] and therefore predicts zero energy for all Zn and Te clusters. The Tersoff potential, on the other hand, predicts energy trends for Zn and Te clusters dramatically different

from DFT. Most seriously, it predicts numerous clusters to have lower energies than the lowest-energy clusters determined from DFT for both Zn and Te. Tersoff and SW potentials do seem to do a reasonable job at capturing the energy trends of the few ZnTe clusters shown in Fig. 1. Unfortunately, without transferability of elemental environments, neither potential will effectively model locally nonstoichiometric situations, i.e. defects and surfaces.

For numerical reference of real values, the unnormalized cohesive energies for representative Zn, Te, ZnTe, and CdZn clusters are compared in Table V of Appendix B. Indeed, BOP is seen to improve over SW and Tersoff potentials on real property values. There are some differences between BOP and DFT or experimental values. It should also be noted that there are differences between our DFT data and data from other groups, as well as between DFT and experiments. Our DFT calculations use the DFT-D method[48,49] as it gives more accurate cohesive energies and bulk moduli for the CdZnTe compounds. We point out that, for the BOP potential, the relation between bond energy and bond length for the nearest neighbor structures always satisfies Eq. (19). This means that energies of clusters and lattices cannot be independently fitted, and hence a tradeoff is made to capture the more important lattices (to be discussed below). This problem also exists for Tersoff potential (which has a similar bond energy vs bond length relation)[50] and is even more obvious for SW potentials. For example, the angular term vanishes for both the dimer and dc structures in SW potentials. This means that the nearest neighbor structures such as dime and dc would have the same bond energy, in contrast with the DFT data. Again, it should be noted that DFT does not necessarily represent experiments, and it is the energy trends, not the absolute values, that will play the most important role in capturing the material dynamics.

Tables VI to IX of Appendix B additionally compare the relaxed geometries for selected Zn, Te, ZnTe, and CdTe clusters. Tables VI and VII indicate that, compared with DFT, the BOP underpredicts the bond lengths of Zn clusters by 4–22%, but overpredicts the bond length of Te clusters by 5–9%. Tables VIII and IX indicate that the bond lengths of ZnTe and CdZn clusters, predicted by the BOP, also deviate from DFT values by 0.3–31% and 6–33%, respectively. As discussed in our previous work,[16] the bond energy vs bond length relation of different (nearest neighbor) structures always satisfies Eq. (19) if ϕ and β_σ are pair functions. Regardless of the parameters, the bond energy specified by Eq. (19) monotonically increases as a function of bond length. In contrast, the DFT bond energy vs bond length data is rather scattered. As a result, it is necessary that some differences will exist between BOP and DFT. Clearly, while the relatively good energy trends of clusters are a significant advantage of BOP over other potentials, better description of the geometries of clusters requires consideration of the environment dependence of the repulsive and bonding functions, i.e. no longer treating the ϕ and β_σ as pair functions.

B. Bulk lattice structures

Based upon BOP and literature SW[39] and Tersoff[40] potentials for Zn-Te, zero-pressure energy minimization simulations[51] are performed to determine the relaxed structures and properties of a variety of Zn, Te, ZnTe, CdZn, and $Cd_{1-x}Zn_xTe$ lattices with coordination numbers between four and 12. Figures 2(a) and 2(b) compare the cohesive energies and atomic volumes (can be related to lattice constants), respectively. To again focus on trends, energies and volumes shown in Fig. 2 are normalized by the magnitude of the energy and volume of the experimentally observed equilibrium structures for Zn, Te, and ZnTe.[42,52] No experimental data exists for CdZn because it is not a stable phase.[53,54] As a result, we normalize the energies and volumes by the corresponding lowest energy phase as determined from DFT.

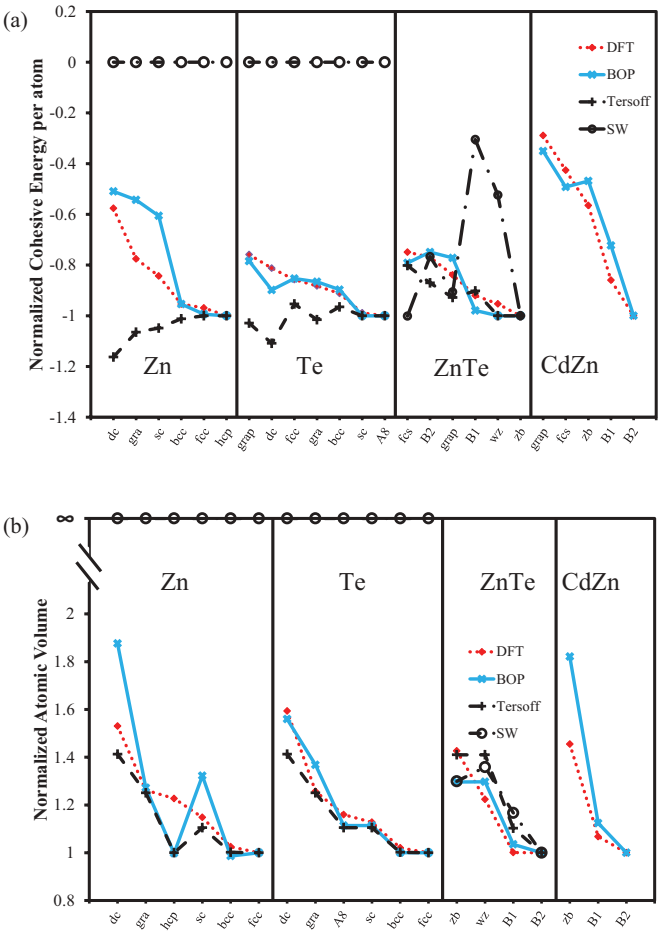

FIG. 2. (Color online) (a) Normalized cohesive energies per atom and (b) normalized volume per atom for selected Zn, Te, ZnTe, and CdZn lattices. Lattices include diamond-cubic (dc), graphite (gra), simple-cubic (sc), base-centered-cubic (bcc), face-centered-cubic (fcc), hexagonal-close-packed (hcp), graphene (grap), γS8 (A8), face-centered-square (fcs), NaCl (B1), CsCl (B2), and wurtzite (wz).

It can be seen from Fig. 2(a) that the BOP almost perfectly captures the energy trends of DFT with the only exceptions that dc-Te, fcs-ZnTe, and fcs-CdZn energies are a little too negative to stay in the DFT energy sequences. Most importantly, BOP correctly captures the hcp-Zn, A8-Te, zb-ZnTe, and B2-CdZn as the lowest energy phases with an almost exact match of their cohesive energies to the available experimental[42,52] or DFT values in Tables X through XII. These significantly improve over the literature potentials. For example, the SW potential cannot model the elemental Zn and Te phases as

the interactions are repulsive, resulting in zero energy and infinite bond length (or atomic volume). Even assuming that structures remain as a ZnTe-zb compound without direct Zn-Zn and Te-Te interactions during dynamics simulations (which is hardly true at high temperatures), the SW potential still does not have energy trends close enough to the DFT data to produce accurate results. Most seriously, the zinc-blende equilibrium phase may not be even stable during simulations as the SW potential predicts the fcs phase to have a lower energy. Compared with DFT, the Tersoff potential predicts monotonic opposite energy trends for Zn and overall opposite trends for Te, both leading to a wrong conclusion that the dc lattice has the lowest energy for the two elements. The Tersoff potential does predict ZnTe energy trends close to DFT with the correct lowest energy ZnTe phase. However, caution should be taken in applying the Tersoff potential. First, Fig. 2(a) only tests a limited number of lattice phases, and it is unclear if the zb lattice has the lowest energy against all other possible lattice and cluster configurations. Second, the potential is not transferrable to elemental environments due to the wrong elemental energy trends and certainly cannot be applied for scenarios where the elemental environments are encountered (e.g. vapor deposition).

Literature ZnTe potential does not include Cd-Zn interactions, and literature CdZn potentials are only applied for metal systems.[55] Hence, no comparison is made with other potentials for the CdZn phases.

Figure 2(b) indicates that, except for a relatively large underestimation of the atomic volume of the hcp Zn, the atomic volume trends predicted by the BOP for the Zn, Te, ZnTe, and CdZn phases actually match the DFT data pretty well. The large deviation for the hcp Zn atomic volume occurs because the hcp Zn lattice has a lattice constant ratio of $c/a = 1.855$,[44] significantly larger than the ideal ratio of 1.633. With extensive efforts, we discovered that BOP could not fit a c/a ratio significantly above the ideal ratio, consistent with the previous work on Cd.[16] As a result, we could not fit a bigger atomic volume for the hcp Zn phase while ensuring other property trends. Note that this issue is not specific to BOP; it also occurs for other potentials.[15,16] However, a more advanced BOP that incorporates the environmental dependence in ϕ and β_σ of Eq. (19) can possibly resolve this problem.[16]

The SW potential predicts infinite atomic volume for elements Zn and Te due to repulsive Zn-Zn and Te-Te interactions. The Tersoff potential, on the other hand, predicts atomic volume trends close to the DFT calculations. Unfortunately, accurate description of atomic volumes becomes irrelevant when a potential does not capture the energy trends to enable a correct dynamic simulation.

For numerical reference, the unnormalized cohesive energies and lattice constants are all listed in Tables X through XIV of Appendix B for Zn, Te, ZnTe, CdZn, and $Cd_{1-x}Zn_xTe$ lattices, respectively. Tables X through B-VIII further confirm that the BOP not only captures good property trends for different lattices of elements and compounds, but also predicts real energy and lattice constant values closer to the DFT calculations than the two literature potentials for most of the lattices, especially the more important low-energy phases. Note that CdZn is not an equilibrium compound, and no experimental properties exist for the metallic $Cd_{0.5}Zn_{0.5}$ alloy (here, subscripts are added to indicate the alloy composition). In fact, $Cd_{0.5}Zn_{0.5}$ alloy phase separates to near Cd and near Zn alloys,[53,54] indicating that positive heat of mixing for CdZn lattices is a more important validation of the BOP potential. Hence, we evaluate CdZn heat of mixing using the data listed in Table XIII.

Heat of mixing represents the energy difference between an alloy or compound and its constituent elements. For an $A_{1-x}B_x$ binary alloy, for instance, the heat of mixing is defined as $\Delta H = E_{c,AB} - [(1-x)\cdot E_{c,A} + x \cdot E_{c,B}]$, where $E_{c,AB}$ is the cohesive energy of the alloy or the compound, and $E_{c,A}$ and $E_{c,B}$ refer to the cohesive energies of the lowest-energy structure of elements A and B, respectively. First, we validate that the BOP predicts correctly a cohesive energy of -1.135 eV/atom for the equilibrium hcp Cd,[16] and a cohesive energy of -1.325 eV/atom for the equilibrium hcp Zn,[42] Table X. Based on these elemental cohesive energies, we can confirm that all of the CdZn structures examined in Table XIII have positive heats of formation, which is in good agreement with the experimental observation that CdZn phase separates.

Lattice constant and cohesive energy as a function of composition x of the $Cd_{1-x}Zn_xTe$ ternary alloy is important to capture. Studying the configurations and distributions of species in a large $Cd_{1-x}Zn_xTe$ crystal requires using either Monte Carlo techniques, with a large number of steps, or MD simulations large enough to have a reasonable number of random and different local configurations to sample the composition phase space. This problem, however, can be well addressed by using BOP and DFT calculations to examine trends of cohesive energies and lattice constants of various compounds,[56] including CdTe, Cd_3ZnTe_4 sulvanite, $CdZnTe_2$ tetragonal $p4m2$, $CdZn_3Te_4$ sulvanite, and ZnTe. The results of these calculations are compared in Table XIV and Fig. 3. It can be seen that BOP predicts increasing lattice constant and decreasing energy with decreasing Zn content, in good agreement with the trends of the DFT calculations. Bond-order potential has been fitted to and captures the experimental CdTe and ZnTe zb cohesive energy while DFT results differ from the experimental values. In addition, both DFT and BOP predict positive heats of formation for all three compounds in the pseudobinary system $Cd_{1-x}Zn_xTe \leftrightarrow (1-x)\,CdTe + x\,ZnTe$, suggesting that the compounds will phase separate into CdZn and ZnTe phases.

Finally, single-crystal elastic constants of the ZnTe-zb phase obtained from BOP and literature experiments[57] are compared in Table XV. It can be seen that BOP captures the elastic constants of the ZnTe-zb phase reasonably well. Note that the parameterization of BOP does not fit the elastic constants, and the agreement with experiments exemplifies the transferability of the BOP model.

C. Melting temperature

Melting temperature simulations test a large number of thermally activated configurations and have implications on modeling thermodynamic properties. Thus, we calculated the melting temperature of the ZnTe-zb phase. We adopted the MD technique proposed by Morris *et al.*[58] with the same procedure outlined in our previous publication.[15,16] We find that the BOP predicts a ZnTe melting temperature of 2050 K. Compared

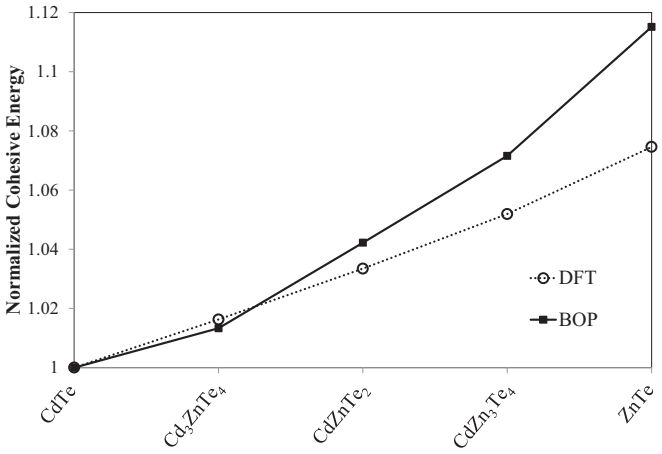

FIG. 3. Normalized cohesive energies for various CdZnTe compounds.

with the 1568 K measured in experiments,[59] the predicted melting temperature is reasonable as the deviation is consistent with the Si Tersoff potential,[60] and our previous result for CdTe[16] that the CdTe BOP predicts a melting temperature of 1550–1600 K as compared with the experimental value of 1365 K. At low temperatures, simulated temperature can be scaled to the real temperature using a quantum correction technique.[61,62] This method, however, does not apply for higher temperatures for which quantum effects are negligible. For higher-temperature simulations, it is important to note that kinetic processes in condensed matters are determined by the thermodynamic and kinetic properties (e.g. diffusion energy barrier) but not directly for the melting temperature. As demonstrated with SW potentials,[35] it is possible to capture thermodynamic and kinetic properties of condensed matters without capturing the melting temperature.[63–65] Hence, our BOP can be reliably used to study condensed matters. For scenarios where melting temperature needs to be specifically addressed, previous work often uses the homologous temperature (T/T_m) to garner important information comparable to experiments.[66–68] Use of a homologous temperature scales the simulated temperature by a factor of $T_{m,\mathrm{exp}}/T_{m,\mathrm{MD}}$, where $T_{m,\mathrm{exp}}$ and $T_{m,\mathrm{MD}}$ refer, respectively, to the experimental and simulated melting temperatures. The homologous temperature works well when melting temperature is known, as for the cases of CdTe and ZnTe. For alloys, such as $Cd_{1-x}Zn_xTe$, a linear dependence of melting temperature on composition x can be used to extract the melting temperature (more accurately, the median between liquidus and solidus lines),[68] yet using homologous temperature scaling is limited to homogenous representative systems. Simulations containing both CdTe- and ZnTe-rich regimes will not necessarily translate to a single real T.

D. ZnTe point defects

As established previously,[16] the Cd-Zn-Te BOP predicts good defect properties for the CdTe-zb phase. Studying defect properties in ZnTe-zb crystals further tests the transferability of the Cd-Zn-Te BOP potential. Various types of defects can be easily introduced in a ZnTe-zb computational crystal. The stoichiometry of the system containing the defects, however, does not necessarily equal the stoichiometry of the perfect crystal. Following the methodology of Zhang and Northrup,[69,70] the defect energy Γ is calculated as a function of the chemical potential difference $\Delta\mu$ as

$$\Gamma = E'_D - 0.5\,(n_{Zn} - n_{Te}) \cdot \Delta\mu, \tag{22}$$

where n_{Zn} and n_{Te} are numbers of Zn and Te atoms in the defective system, E'_D is an intrinsic defect energy at the stoichiometric condition, and $\Delta\mu$ is the chemical potential difference characteristic of the stoichiometry of the environment. Here, $\Delta\mu$ is expressed as

$$\Delta\mu = \left(\mu_{Zn} - \mu_{Zn}^{\mathrm{bulk}}\right) - \left(\mu_{Te} - \mu_{Te}^{\mathrm{bulk}}\right), \tag{23}$$

where μ_{Zn} and μ_{Te} are the chemical potentials of Zn and Te in the ZnTe compound, and μ_{Zn}^{bulk} and μ_{Te}^{bulk} are the chemical potentials for the lowest-energy Zn and Te phases. In our work, all chemical potentials are approximated as cohesive energies per atom unit. Under the equilibrium condition, $\Delta\mu$ satisfies the condition $-\Delta H_f < \Delta\mu < \Delta H_f$, where ΔH_f is heat of formation.[70] In general, $\Delta\mu = 0$, $\Delta\mu > 0$, and $\Delta\mu < 0$ mean stoichiometric, Zn-rich, and Te-rich conditions.

The intrinsic defect energy can be calculated as

$$\begin{aligned} E'_D = {} & E_D - 0.5\,(n_{Zn} + n_{Te}) \cdot \mu_{ZnTe}^{\mathrm{bulk}} \\ & - 0.5\,(n_{Zn} - n_{Te}) \cdot \left(\mu_{Zn}^{\mathrm{bulk}} - \mu_{Te}^{\mathrm{bulk}}\right), \end{aligned} \tag{24}$$

where E_D is the total energy of the system containing the defect, and $\mu_{ZnTe}^{\mathrm{bulk}}$ is the chemical potential of the lowest-energy ZnTe phase. Under the stoichiometric condition, $\Delta\mu = 0$ and $E'_D = \Gamma$. Under the Zn- or Te-rich condition, $\Delta\mu \neq 0$ and thus $E'_D \neq \Gamma$.

The ZnTe defects considered here include Zn vacancy (V_{Zn}), Te vacancy (V_{Te}), Zn at Te antisite (Zn_{Te}), Te at Zn antisite (Te_{Zn}), Zn interstitial surrounded by the Te and Zn tetrahedron shells (notated as $Zn_{i,Te}$ and $Zn_{i,Zn}$, respectively), and Te interstitial surrounded by the Zn and Te tetrahedron shells (notated as $Te_{i,Zn}$ and $Te_{i,Te}$, respectively). In addition, Zn and Te $\langle 110\rangle$ and $\langle 100\rangle$ dumbbell interstitials[71] (notated as $Zn_{i,\langle 110\rangle}$, $Zn_{i,\langle 100\rangle}$, $Te_{i,\langle 110\rangle}$, and $Te_{i,\langle 100\rangle}$), are also considered. The dumbbell interstitials are formed by splitting an on-site Zn or Te atom into two atoms with their bond aligned along either the $\langle 100\rangle$ or $\langle 110\rangle$ direction.[71,72]

Energy minimization simulations are performed to calculate the total energies E_D of the ZnTe-zb systems (with about 512 atoms) containing the corresponding defects. The intrinsic defect energies are then calculated using Eq. (24), and the results obtained for DFT, BOP, and the ZnTe Tersoff potential[40] are shown in Fig. 4. Here, the SW potential is not studied as it incorrectly defines repulsive interactions for elemental Zn and Te and therefore cannot be applied for defects. For numerical references, defect energies are also given in Table XVI.

Figure 4 and Table XVI indicate that the two lowest-energy defects predicted by the DFT calculations are the two Zn interstitials $Zn_{i,\langle 110\rangle}$ and $Zn_{i,Zn}$, and BOP slightly overestimates the energies of these two defects. However, BOP captures very well DFT energy trends of the next eight lowest-energy defects V_{Te}, $Zn_{i,Te}$, V_{Zn}, Te_{Zn}, $Zn_{i,\langle 100\rangle}$, $Te_{i,\langle 100\rangle}$, $Te_{i,Zn}$, and $Te_{i,\langle 110\rangle}$, with an exact match of the V_{Te} energy. The fact

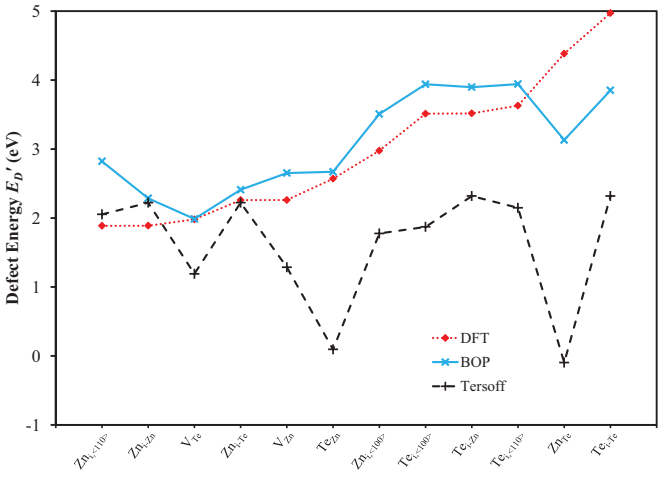

FIG. 4. (Color online) Various defect energies of the ZnTe-zb phase.

that Zn vacancy is among the defects accurately captured by the BOP is important because the primary native defects observed in ZnTe compounds are attributed to Zn vacancies under Te-rich conditions.[73–75] The Tersoff potential not only does not capture the defects energy trends, but also predicts that the Te_{Zn} and Zn_{Te} antisites have much lower energies than the lowest-energy defect in the DFT calculations. Most seriously, the Tersoff potential indicates a negative energy for the Zn_{Te} antisites, suggesting that the Tersoff potential cannot even be used in MD simulation to study a ZnTe crystal as the system is not stable. This further indicates that a valid potential must be tested under a variety of conditions including defects. Merely capturing energy trends of a few lattice phases, as illustrated in Fig. 2(a) for the Tersoff potential of ZnTe lattices, does not guarantee that potential can be used for these phases. Bond-order potential accurately captures energies of many defects, a clear advantage over other potentials.

E. ZnTe surfaces

Surface reconfigurations provide additional tests of the transferability of an interatomic potential. Previous work[16] has verified that the Cd-Zn-Te BOP captures well the (010) CdTe-zb surface reconstructions. To further evaluate the transferability of our BOP, we study the (010) ZnTe-zb surface. The (010) surface of the ZnTe-zb crystal exhibits a variety of surface reconstructions depending on the environment.[76,77] Figure 5 shows some reported[76,77] and postulated surface reconstructions. Experiments by Feldman[76] showed that a moderate Zn:Te vapor flux ratio environment leads to a Te (2×1) reconstruction. Increasing the Zn:Te flux ratio causes a combination of Te (2×1) and Zn c(2×2) reconstructions. Experiments by Daudin *et al.*[77] show that the Te c(2×2) reconstruction (Te coverage of $\xi = 1.0$) is favorable under Te-rich environments, and the Zn c(2×2) reconstruction (Te coverage $\xi = 0.5$) is favorable under Zn-rich environments.

Energy minimization simulations are used to calculate total energies of the relaxed systems containing various surface reconstructions. The computational cell contains a block of zb ZnTe crystal with ~2300–2500 atoms. The simulations employ periodic boundary conditions in the x and z directions with two parallel free surfaces (of the same reconstructions) created in the $+/-y$ directions. The two surfaces are not perfectly symmetric as one of the free surfaces is rotated 90° relative to the opposite surface. Based on the relaxed total energies, Eq. (22) is used to calculate surface energies as a function of the chemical potential difference $\Delta\mu$, Eq. (23) for all 10 ZnTe-zb (010) surface reconstructions shown in Fig. 5. Here, $\Delta\mu$ is left as an independent variable representing transition from Te- to Zn-rich environments. The calculated surface energies, results of Eq. (22) divided by the number of surface unit cells (Fig. 5) in the simulation, are summarized in Figs. 6(a) and 6(b) for the BOP potential and DFT, respectively. Figure 6(a) indicates that, within the possible range of chemical potential difference between $-\Delta H_f$ and ΔH_f, the BOP predicts the preferred surface as Te (2×1) (coverage $\xi = 1.0$) and Te c(2×2) (coverage $\xi = 1.5$) in the Te-rich environments ($\Delta\mu$ near the $-\Delta H_f$ end), in good agreement with experiments.[76,77] This is also consistent with DFT results depicted in Fig. 6(b) showing the Te (2×1) (coverage $\xi = 1.0$) as the preferred surface in the Te-rich condition. In addition, Fig. 6(a) shows that in the Zn-rich environments ($\Delta\mu$ near the ΔH_f end), the preferred surface predicted by the BOP is Zn (1×2) (coverage $\xi = 1.0$). On the other hand, DFT indicates Zn (2×1) and Zn c(2×2) (both with coverage $\xi = 0.5$) as the preferred surfaces in Zn-rich environments, which differs from the BOP result. These observations, require that $\Delta\mu$ is strictly constrained between $-\Delta H_f$ and ΔH_f, which is true under experimental equilibrium condition. However, under highly nonequilibrium conditions typically used in MD, the Zn-rich condition may reach $\Delta\mu \gg \Delta H_f$. Then the DFT calculations would predict Zn (1×2) (coverage $\xi = 1.0$) as the lowest energy surface, in agreement with the BOP. These results indicate that, while there are some differences from the DFT, the BOP-based simulations can still capture the fundamental physics involving surface reconstructions.

F. Vapor deposition simulations

As mentioned above, vapor deposition simulations are extremely important because they test configurations that cannot be tested otherwise. Previous work[16] has validated that our Cd-Zn-Te ternary BOP captures the crystalline growth of Cd, Te, and CdTe during MD vapor deposition simulations. Here, we further perform MD vapor deposition simulations to validate Zn-hcp, $Cd_{0.5}Zn_{0.5}$-hcp alloy, ZnTe-zb, and $Cd_{0.5}Zn_{0.5}$Te-zb growth. Our computational systems employ periodic boundary conditions in the x and z directions and a free boundary condition in the y direction. The growth occurs in the $+y$ direction, with a constant zero pressure maintained during simulations to relax the system dimensions.

For Zn growth, an initial substrate of an hcp crystal containing 3072 Zn atoms with 24 $(2\bar{1}\bar{1}0)$ layers in the x direction, eight (0002) layers in the y direction, and 16 $(0\bar{1}10)$ layers in the z direction is used, where layers refer to crystallographic planes so that one (0001) layer is equivalent n $(000n)$ layers, etc. The substrate temperature is set at $T = 400$ K by assigning velocities to atoms according to the

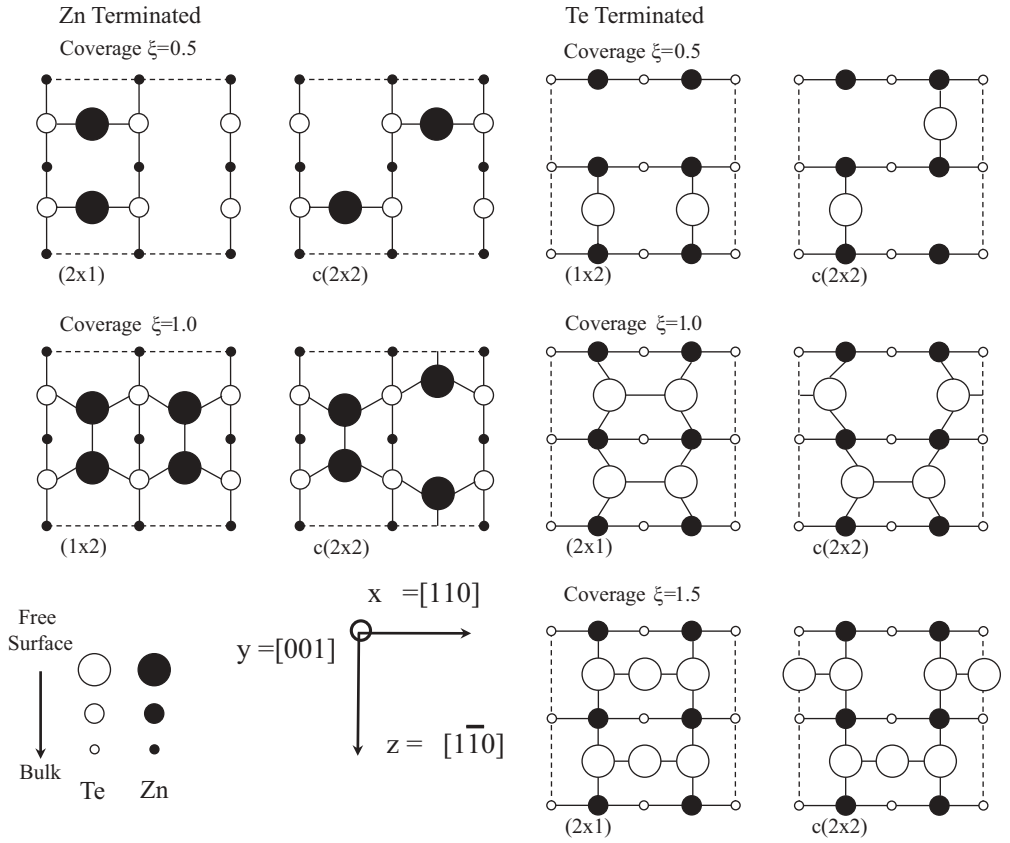

FIG. 5. Possible surface reconstructions on (010) ZnTe-zb.

Boltzmann distribution. During simulations, the bottom $(-y)$ two (0002) layers are held fixed to prevent crystal shift upon adatom impact on the top surface. The next three (0002) layers are isothermally controlled at the substrate temperature. This leaves the top three layers free where the motion of atoms is solely determined by Newton's law. Injection of Zn adatoms from random locations far above the surface simulates the growth. All adatoms have an initial far-field incident kinetic energy $E_i = 0.1$ eV and an incident angle $\theta = 0^o$ (i.e. the moving direction is perpendicular to the surface). The adatom injection frequency is chosen to give a deposition rate of $R = 2.2$ nm/ns. To approximately maintain a constant thickness of the free surface region, the isothermal region expands upward during simulations. Since surface roughness might develop, the isothermal region expands at about 80% of the surface growth rate so that the upper boundary of the isothermal region never exceeds the surface even at the valley locations. Figure 7 depicts the resulting configuration obtained after 0.42 ns deposition. Note that, in Figs. 7–11, the original substrate is shaded in yellow. Figure 7 shows that the BOP correctly captures the crystalline growth of the Zn.

For $Cd_{0.5}Zn_{0.5}$ growth, we create an initial substrate of an hcp $Cd_{0.5}Zn_{0.5}$ alloyed crystal containing 1520 Cd atoms and 1552 Zn atoms with 24 $(2\bar{1}\bar{1}0)$ layers in the x direction, eight (0002) layers in the y direction, and 16 $(0\bar{1}10)$ layers in the z direction. The spatial distributions of the Cd and Zn atoms are random. This vapor deposition simulation utilizes the same approach as described above at a substrate temperature $T = 300$ K, an incident energy $E_i = 0.1$ eV, an incident angle $\theta = 0^o$, a deposition rate $R = 2.6$ nm/ns, and a vapor flux ratio Cd:Zn = 1:1 (while randomly chosen, the adatom species will eventually average to approximately 50% Cd and 50% Zn). Figure 8 shows the resulting configuration obtained after 0.42 ns deposition. It can be seen from Fig. 8 that the deposited region contains significantly distorted local regions that are not perfectly crystalline. It is recognized that, unlike the equilibrium phases Zn-hcp, ZnTe-zb, and $Cd_{0.5}Zn_{0.5}$Te-zb, the $Cd_{0.5}Zn_{0.5}$-hcp phase is not an equilibrium phase. It has a positive heat of mixing and decomposes into Cd- and Zn-rich phases in experiments. The fast deposition rates employed in MD simulations do not provide significant time for this phase separation to fully complete. As a result, it is expected that the unstable $Cd_{0.5}Zn_{0.5}$-hcp phase evolve towards defective regions during MD vapor deposition simulations. Figure 8, therefore, confirms that our BOP correctly predicts a nonequilibrium $Cd_{0.5}Zn_{0.5}$ alloyed phase.

For ZnTe growth, an initial substrate of a zb crystal containing 1008 Zn atoms and 1008 Te atoms with 24 (101) layers in the x direction, 12 (040) layers in the y direction, and seven $(\bar{1}01)$ layers in the z direction is used. Initially, Zn terminates the top y surface. During simulations, the bottom three (040) layers are held fixed. To mimic the molecular beam epitaxy (MBE) growth condition commonly used for semiconductor growth, we expanded the isothermal region to include all atoms above the fixed region. To capture the adatom incident energy effects, however, the simulation does

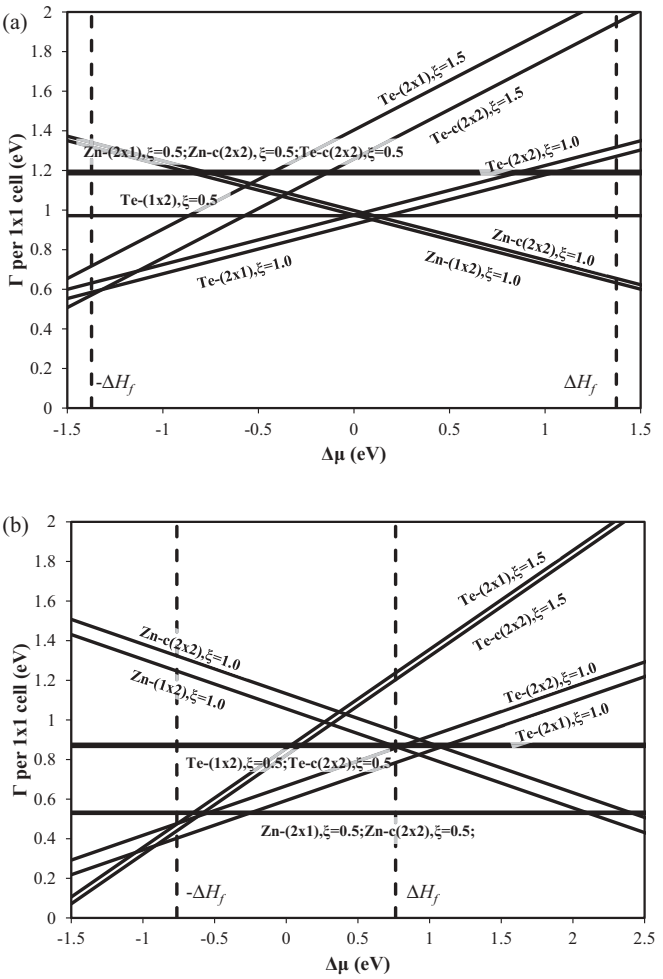

FIG. 6. (010) ZnTe surface energy phase diagrams predicted by (a) BOP and (b) DFT.

not isothermally control the newly added adatoms until they fully incorporate into the film and their initial kinetic and potential (latent heat release) energies fully dissipate. The

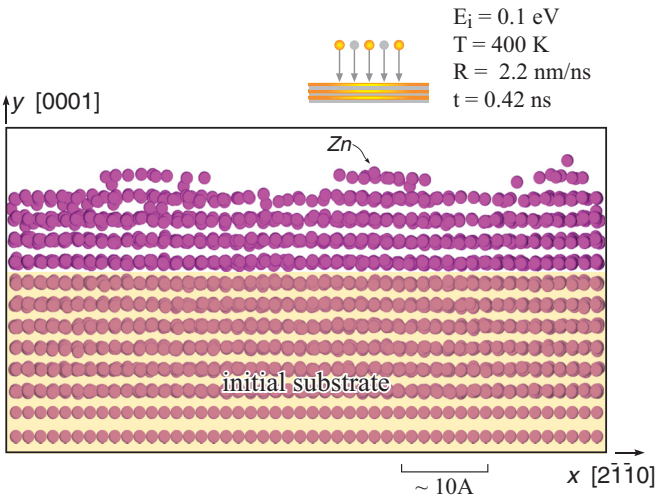

FIG. 7. (Color online) Growth of hcp Zn in the [0001] direction (initial substrate is shaded in yellow) predicted by BOP.

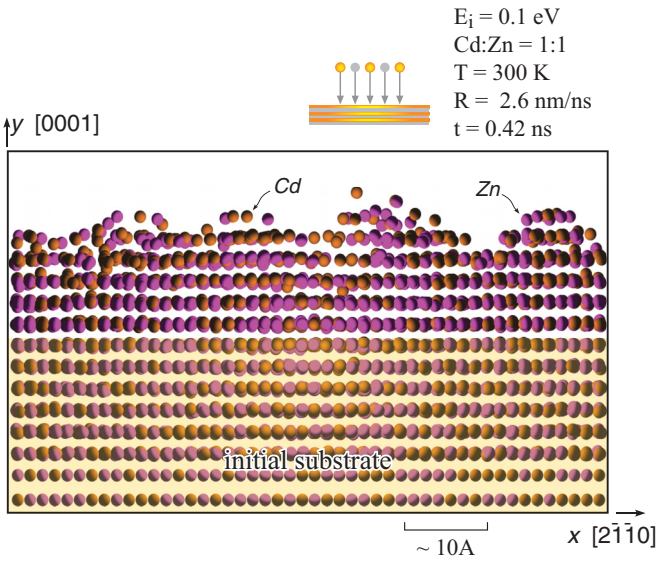

FIG. 8. (Color online) Growth of hcp $Cd_{0.5}Zn_{0.5}$ alloy in the [0001] direction (initial substrate is shaded in yellow) predicted by BOP.

growth simulation has a substrate temperature $T = 1200$ K, an incident energy $E_i = 0.1$ eV, an incident angle $\theta = 0^o$, a deposition rate $R = 2.4$ nm/ns, and a stoichiometric vapor flux ratio Zn:Te = 1:1. Figure 9 depicts the system configuration obtained at 1.2 ns deposition time. It is seen again that our BOP correctly captures the crystalline growth of the equilibrium ZnTe-zb crystal.

As mentioned above, vapor deposition tests are largely ignored in previous semiconductor potential development. To understand the performance of the potentials that do not consider vapor deposition in their parameterization, the literature SW[39] and Tersoff[40] Zn-Te potentials are also used in vapor deposition simulations. As expected from the incorrect

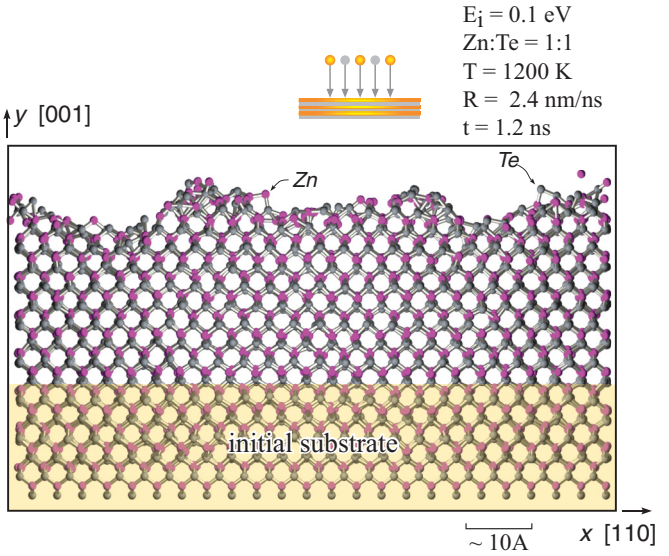

FIG. 9. (Color online) Growth of zb ZnTe in the [010] direction (initial substrate is shaded in yellow) predicted by BOP.

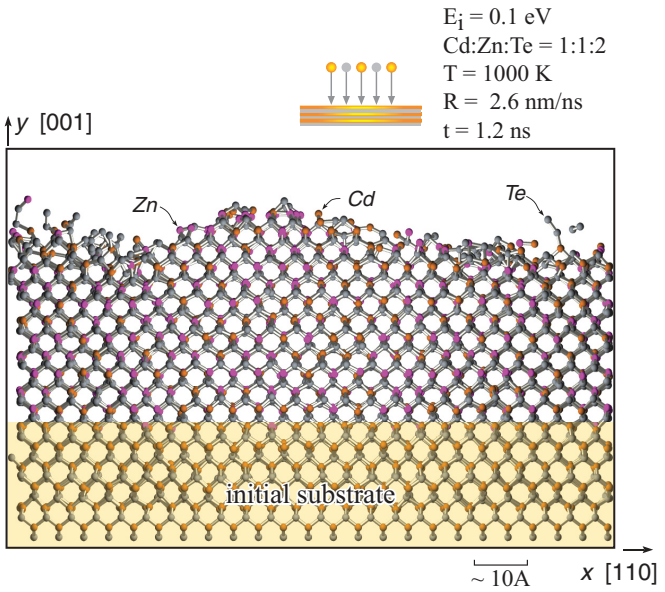

FIG. 10. (Color online) Growth of zb $Cd_{0.5}Zn_{0.5}Te$ alloy in the [010] direction (initial substrate is shaded in yellow) predicted by BOP.

repulsive Zn-Zn and Te-Te interactions, we find that the SW potential predicts an amorphous growth, which is not further discussed here. Our calculation indicates that the Tersoff Zn-Te potential predicts a melting temperature of (∼1200 K) for ZnTe. As a result, we perform vapor deposition simulation of ZnTe at 800 K. We find that the predicted film has an alloyed diamond-cubic structure as opposed to the correct zinc-blende structure. This is consistent with Fig. 2(a) that the Tersoff potential predicts the dc phase as the lowest energy for both Zn and Te. Again, this clearly indicates that vapor deposition simulations are extremely effective for testing the transferability of an interatomic potential, and the wrong properties of elements are reflected in compound simulations.

For $Cd_{0.5}Zn_{0.5}Te$ growth, we begin with a zb CdTe substrate containing 864 Cd atoms and 864 Te atoms with 24 (101) layers in the x direction, 12 (040) layers in the y direction, and six ($\bar{1}01$) layers in the z direction. Initially, Cd atoms terminated the surface. Following the same approach used for ZnTe, the $Cd_{0.5}Zn_{0.5}Te$ growth is simulated at a substrate temperature $T = 1000$ K, an incident energy $E_i = 0.1$ eV, an incident angle $\theta = 0^o$, a deposition rate $R = 2.6$ nm/ns, and a vapor flux ratio Cd:Zn:Te = 1:1:2. Figure 10 shows the configuration obtained at 1.2 ns deposition time. It again validates that our BOP correctly captures the crystalline growth of the ternary zb $Cd_{0.5}Zn_{0.5}Te$ commonly achieved in experiments. Note that, here, we actually simulate a more complicated $Cd_{0.5}Zn_{0.5}Te$/CdTe multilayer growth.

The past successful MD simulations of crystalline growth of equilibrium semiconductor crystals are achieved primarily using SW potentials. The problem is that SW potentials only stabilize the tetrahedral structure without capturing the property trends of other configurations, and as a result they predict wrong defect information. Without including growth simulation tests in parameterizations, many literature Tersoff potentials do not predict crystalline growth.[15,33,34] Even when a Tersoff potential does predict crystal growth it is not guaranteed that the correct stoichiometry is retained. This work develops Cd-Zn-Te ternary BOP that is fundamentally more transferrable than Tersoff potentials. More importantly, we demonstrate that well-parameterized BOP can simultaneously capture property trends of a variety of phases and crystalline growth of the equilibrium phases under a variety of chemical conditions. It is the improved property trends and crystalline simulation capability that distinguish our Cd-Zn-Te BOP from previous potentials. This also highlights how BOP has made a significant stride toward improving semiconductor simulations, which can change future theoretical studies of materials.

V. CONCLUSIONS

We have developed a high-fidelity BOP for the Cd-Zn-Te ternary system. Unlike other semiconductor potentials currently available, this BOP simultaneously meets three criteria: (a) It is derived directly from quantum mechanical theories and hence is likely to be transferrable to environments that are not explicitly tested. (b) It accurately captures property trends of many configurations including defects and surfaces. (c) Most importantly, it results in crystalline growth in MD vapor deposition simulations under a variety of chemical conditions. We achieved high-quality parameterization by considering a large number of target structures with coordination ranging from 2 to 12; setting physically valid bounds for all parameters; applying the two-step fitting approach; using different minimization schemes; and iterating the parameterization with crystalline growth simulation tests.

The BOP approach will enable empirical MD simulations of semiconductors to achieve a fidelity level approaching the quantum mechanical methods. As a demonstration in a ternary system, our Cd-Zn-Te BOP enables accurate study of $Cd_{1-x}Zn_xTe$ semiconductor compounds. Equally important, our work highlights a BOP framework where new elements can be continuously added into existing BOPs while retaining the fidelity of the previous systems. This will enable easy extension of the BOP and the possibility of combining BOPs developed by different authors for studying future semiconductor systems with increasing complexity.

ACKNOWLEDGMENTS

This work is supported by the NNSA/DOE Office of Nonproliferation Research and Development, Proliferation Detection Program, Advanced Materials Portfolio. Sandia National Laboratories is a multiprogram laboratory managed and operated by Sandia Corporation, a wholly owned subsidiary of Lockheed Martin Corporation, for the US Department of Energy's National Nuclear Security Administration under contract DE-AC04-94AL85000.

APPENDIX A: PARAMETER BOUNDS

TABLE IV. Bounds on BOP parameters.

Elemental Zn
$1.0 < 1.99 \cdot n_{ZnZn} < m_{ZnZn} < 2.01 \cdot n_{ZnZn} < 4$
$0.05 < 8 \cdot \beta_{\pi,0,ZnZn} < \beta_{\sigma,0,ZnZn} < 0.8 \cdot \phi_{0,ZnZn} < 0.8$
$n_{c,ZnZn} = 2.8$
$n_{ZnZn} > \frac{\ln(\xi)}{\ln\left[\exp\left(1-\ell^{n_{c,ZnZn}}\right)/\ell\right]}, \xi = 0.05, \ell = 1.5$
$0.42 \leqslant p_{\pi,Zn} \leqslant 1$
$\beta^2_{\pi,0,ZnZn} \leqslant p_{\pi,Zn} \cdot \beta^2_{\sigma,0,ZnZn}$
$0 \leqslant \beta_{\sigma,0,ZnZn} \leqslant 8$
$0 \leqslant \beta_{\pi,0,ZnZn} \leqslant 8$
$0 \leqslant c_{\sigma,ZnZn} \leqslant 3.65$
$0.2 \leqslant f_{\sigma,ZnZn} \leqslant 0.8$
$-15 \leqslant k_{\sigma,ZnZn} \leqslant 15$
$0 < b_{\sigma,ZnZnZn} \leqslant 1$
$-0.4 \leqslant u_{\sigma,ZnZnZn} \leqslant 0.2$
$(b_{\sigma,ZnZnZn} + g_{0,ZnZnZn})^2 \left(u^2_{\sigma,ZnZnZn} - 1\right)^2 > 4[g_{0,ZnZnZn} - b_{\sigma,ZnZnZn} + (g_{0,ZnZnZn} + b_{\sigma,ZnZnZn})u_{\sigma,ZnZnZn}]^2$
Binary CdZn
$0.1 < 1.99 \cdot n_{CdZn} < m_{CdZn} < 2.01 \cdot n_{CdZn} < 4$
$0.05 < 2 \cdot \beta_{\pi,0,CdZn} < \beta_{\sigma,0,CdZn} < 0.8 \cdot \phi_{0,CdZn} < 5.0$
$n_{c,CdZn} = 2.8$
$n_{CdZn} > \frac{\ln(\xi)}{\ln\left[\exp\left(1-\ell^{n_{c,CdZn}}\right)/\ell\right]}, \xi = 0.05, \ell = 1.5$
$\beta^2_{\pi,0,CdZn} \leqslant p_{\pi,Cd} \cdot \beta^2_{\sigma,0,CdZn}$
$\beta^2_{\pi,0,CdZn} \leqslant p_{\pi,Zn} \cdot \beta^2_{\sigma,0,CdZn}$
$0 \leqslant \beta_{\sigma,0,CdZn} \leqslant 2$
$0 \leqslant \beta_{\pi,0,CdZn} \leqslant 1$
$0.8 \leqslant c_{\sigma,CdZn} \leqslant 3.65$
$0 \leqslant f_{\sigma,CdZn} \leqslant 1$
$-20 \leqslant k_{\sigma,CdZn} \leqslant 20$
$0.2 \leqslant b_{\sigma,CdCdZn} \leqslant 1$
$-0.4 \leqslant u_{\sigma,CdCdZn} \leqslant 0.1$
$(b_{\sigma,CdCdZn} + g_{0,CdCdZn})^2 \left(u^2_{\sigma,CdCdZn} - 1\right)^2 \geqslant 4[g_{0,CdCdZn} - b_{\sigma,CdCdZn} + (g_{0,CdCdZn} + b_{\sigma,CdCdZn})u_{\sigma,CdCdZn}]^2$
$0.2 \leqslant b_{\sigma,ZnCdZn} \leqslant 1$
$-0.4 \leqslant u_{\sigma,ZnCdZn} \leqslant 0.1$
$(b_{\sigma,ZnCdZn} + g_{0,ZnCdZn})^2 \left(u^2_{\sigma,ZnCdZn} - 1\right)^2 \geqslant 4[g_{0,ZnCdZn} - b_{\sigma,ZnCdZn} + (g_{0,ZnCdZn} + b_{\sigma,ZnCdZn})u_{\sigma,ZnCdZn}]^2$
$0.2 \leqslant b_{\sigma,CdZnCd} \leqslant 1$
$-0.4 \leqslant u_{\sigma,CdZnCd} \leqslant 0.1$
$(b_{\sigma,CdZnCd} + g_{0,CdZnCd})^2 \left(u^2_{\sigma,CdZnCd} - 1\right)^2 \geqslant 4[g_{0,CdZnCd} - b_{\sigma,CdZnCd} + (g_{0,CdZnCd} + b_{\sigma,CdZnCd})u_{\sigma,CdZnCd}]^2$
$0.2 \leqslant b_{\sigma,CdZnZn} \leqslant 1$
$-0.4 \leqslant u_{\sigma,CdZnZn} \leqslant 0.1$
$(b_{\sigma,CdZnZn} + g_{0,CdZnZn})^2 \left(u^2_{\sigma,CdZnZn} - 1\right)^2 \geqslant 4[g_{0,CdZnZn} - b_{\sigma,CdZnZn} + (g_{0,CdZnZn} + b_{\sigma,CdZnZn})u_{\sigma,CdZnZn}]^2$
Binary ZnTe
$0.1 < 1.99 \cdot n_{ZnTe} < m_{ZnTe} < 2.01 \cdot n_{ZnTe} < 4$
$0.05 < 2 \cdot \beta_{\pi,0,ZnTe} < \beta_{\sigma,0,ZnTe} < 0.8 \cdot \phi_{0,ZnTe} < 5.0$
$n_{c,ZnTe} = 2.8$
$n_{ZnTe} > \frac{\ln(\xi)}{\ln\left[\exp\left(1-\ell^{n_{c,ZnTe}}\right)/\ell\right]}, \xi = 0.10, \ell = 1.5$
$\beta^2_{\pi,0,ZnTe} \leqslant p_{\pi,Zn} \cdot \beta^2_{\sigma,0,ZnTe}$
$\beta^2_{\pi,0,ZnTe} \leqslant p_{\pi,Te} \cdot \beta^2_{\sigma,0,ZnTe}$
$0 \leqslant \beta_{\sigma,0,ZnTe} \leqslant 2$
$0 \leqslant \beta_{\pi,0,ZnTe} \leqslant 1$
$0.8 \leqslant c_{\sigma,ZnTe} \leqslant 3.65$
$0.2 \leqslant b_{\sigma,TeTeZn} \leqslant 1$
$-0.4 \leqslant u_{\sigma,TeTeZn} \leqslant 0.1$
$(b_{\sigma,TeTeZn} + g_{0,TeTeZn})^2 \left(u^2_{\sigma,TeTeZn} - 1\right)^2 \geqslant 4[g_{0,TeTeZn} - b_{\sigma,TeTeZn} + (g_{0,TeTeZn} + b_{\sigma,TeTeZn})u_{\sigma,TeTeZn}]^2$
$0.2 \leqslant b_{\sigma,ZnTeZn} \leqslant 1$
$-0.4 \leqslant u_{\sigma,ZnTeZn} \leqslant 0.1$
$(b_{\sigma,ZnTeZn} + g_{0,ZnTeZn})^2 \left(u^2_{\sigma,ZnTeZn} - 1\right)^2 \geqslant 4[g_{0,ZnTeZn} - b_{\sigma,ZnTeZn} + (g_{0,ZnTeZn} + b_{\sigma,ZnTeZn})u_{\sigma,ZnTeZn}]^2$
$0.2 \leqslant b_{\sigma,TeZnTe} \leqslant 1$
$-0.4 \leqslant u_{\sigma,TeZnTe} \leqslant 0.1$

TABLE IV. (*Continued.*)

$(b_{\sigma,TeZnTe}+g_{0,TeZnTe})^2\left(u^2_{\sigma,TeZnTe}-1\right)^2 \geqslant 4[g_{0,TeZnTe}-b_{\sigma,TeZnTe}+(g_{0,TeZnTe}+b_{\sigma,TeZnTe})u_{\sigma,TeZnTe}]^2$
$0.2 \leqslant b_{\sigma,TeZnZn} \leqslant 1$
$-0.4 \leqslant u_{\sigma,TeZnZn} \leqslant 0.1$
$(b_{\sigma,TeZnZn}+g_{0,TeZnZn})^2\left(u^2_{\sigma,TeZnZn}-1\right)^2 \geqslant 4[g_{0,TeZnZn}-b_{\sigma,TeZnZn}+(g_{0,TeZnZn}+b_{\sigma,TeZnZn})u_{\sigma,TeZnZn}]^2$
Ternary CdZnTe
$0.2 \leqslant b_{\sigma,TeCdZn} \leqslant 1$
$-0.4 \leqslant u_{\sigma,TeCdZn} \leqslant 0.1$
$(b_{\sigma,TeCdZn}+g_{0,TeCdZn})^2\left(u^2_{\sigma,TeCdZn}-1\right)^2 \geqslant 4[g_{0,TeCdZn}-b_{\sigma,TeCdZn}+(g_{0,TeCdZn}+b_{\sigma,TeCdZn})u_{\sigma,TeCdZn}]^2$
$0.2 \leqslant b_{\sigma,CdTeZn} \leqslant 1$
$-0.6 \leqslant u_{\sigma,CdTeZn} \leqslant 0.1$
$(b_{\sigma,CdTeZn}+g_{0,CdTeZn})^2\left(u^2_{\sigma,CdTeZn}-1\right)^2 \geqslant 4[g_{0,CdTeZn}-b_{\sigma,CdTeZn}+(g_{0,CdTeZn}+b_{\sigma,CdTeZn})u_{\sigma,CdTeZn}]^2$
$0.2 \leqslant b_{\sigma,CdZnTe} \leqslant 1$
$-0.4 \leqslant u_{\sigma,CdZnTe} \leqslant 0.1$
$(b_{\sigma,CdZnTe}+g_{0,CdZnTe})^2\left(u^2_{\sigma,CdZnTe}-1\right)^2 \geqslant 4[g_{0,CdZnTe}-b_{\sigma,CdZnTe}+(g_{0,CdZnTe}+b_{\sigma,CdZnTe})u_{\sigma,CdZnTe}]^2$

APPENDIX B: COMPLETE LIST OF PREDICTED PROPERTIES

TABLE V. Cohesive energies (eV/atom) for selected Zn, Te, ZnTe, and CdZn clusters.

Cluster Type	DFT	BOP	SW	Tersoff	Experiment
Zn-di	−0.058	−0.272	0.000	−0.809	−0.017[a]
Zn-ch	−0.982	−0.340	0.000	−1.169	
Zn-sq	−0.122	−0.393	0.000	−1.138	
Zn-tri	−0.139	−0.443	0.000	−0.830	
Zn-rhom	−0.164	−0.523	0.000	−0.971	
Zn-tetra	−0.264	−0.567	0.000	−0.891	
Te-di	−1.790	−1.415	0.000	−0.809	−2.66[b]
Te-ch	−1.872	−1.417	0.000	−1.169	
Te-tri	−1.969	−1.383	0.000	−0.830	
Te-sq	−1.998	−1.462	0.000	−1.138	
Te-rhom	−2.136	−1.462	0.000	−0.971	
ZnTeZn-tri	−0.577	−0.855	−1.619	−0.830	
ZnTe-di	−0.593	−0.721	−1.378	−0.809	−0.412[c]
TeZnTe-tri	−1.259	−1.250	−1.619	−0.830	
ZnTe-rhom	−1.468	−1.256	−1.887	−0.971	
CdZn-di	−0.075 (−0.015[d], −0.020[e])	−0.181			
ZnCdZn-tri	−0.151	−0.324			
CdZnCd-tri	−0.167	−0.296			
CdZn-rhom	−0.187	−0.403			

[a]Experimental data (Ref. 41).
[b]Experimental data (Ref. 42).
[c]Experimental data (Ref. 78).
[d]Literature DFT data (Ref. 79).
[e]Literature DFT data (Ref. 80).

TABLE VI. Geometries of selected Zn clusters.

	DFT		BOP		SW		Tersoff	
Structure	r (Å)	θ (°)	r (Å)	θ (°)	r (Å)	θ (°)	r (Å)	θ (°)
di	3.23 (4.19)[a]		2.51		∞		2.53	
tri	3.10	60.0	2.61	60.0	∞		2.75	60.0
sq	3.21	90.0	2.57	90.0	∞		2.64	90.0
tetra	2.80	60.0	2.68	60.0	∞		2.86	60.0
ch	3.17,3.11	180.0	2.6,2.56	180.0	∞,∞		2.55,2.54	180.0

[a]Experimental data (Ref. 43).

TABLE VII. Geometries of selected Te clusters.

	DFT		BOP		SW		Tersoff	
Structure	r (Å)	θ (°)	r (Å)	θ (°)	r (Å)	θ (°)	r (Å)	θ (°)
di	2.60 (2.56)[b]		2.74		∞		2.53	
tri	2.77	60.0	3.01	60.0	∞		2.75	60.0
sq	2.81	90.0	2.99	90.0	∞		2.64	90.0
ch	2.60, 3.15	180.0	2.74,4.07	180.0	∞,∞		2.55,2.54	180.0

[b]Experimental data (Ref. 81).

TABLE VIII. Geometries of selected ZnTe clusters.

	DFT		BOP		SW		Tersoff	
Structure	r (Å)	θ (°)	r (Å)	θ (°)	r (Å)	θ (°)	r (Å)	θ (°)
di	2.40		2.54		2.44		2.53	
Zn_2Te-tri	2.6, 3.27	51.0, 78.0	2.59, 4.36	63.9, 52.3	2.45, 4.68	146.1, 16.9	2.75	60.0
Te_2Zn-tri	3.74, 4.10	37.9, 63.5	2.78, 2.82	35.2, 72.4	2.45, 4.68	146.1, 16.9	2.75	60.0
rhom[a]	2.55, 2.56	59.1, 120.6	2.74	65.5, 114.5	2.50	75.0, 105.0	2.75	63.2, 116.8

[a]For rhom, the first angle θ centers at Zn, and the second one centers at Te.

TABLE IX. Geometries of selected CdZn clusters.

	DFT		BOP	
Structure	r (Å)	θ (°)	r (Å)	θ (°)
di	3.33 (4.28[a], 4.76[b])		2.60	
Cd_2Zn-tri	3.27,3.39	58.7,62.6	3.09,2.72	63.9,52.3
Zn_2Cd-tri	3.26,3.12	61.4,57.1	2.51,4.15	35.2,72.4
rhom	3.33	60.1,120.2	2.56	65.5,114.5

[a]Literature DFT (Ref. 79).
[b]Literature DFT (Ref. 80).

TABLE X. Zn bulk lattice properties.

	DFT		BOP		SW		Tersoff	
Structure	a,c (Å)	E_c (eV)	a,c (Å)	E_c (eV)	a,c	E_c (eV)	a,c (Å)	E_c (eV)
dc	5.61	−0.835	6.27	−0.675	∞	0.000	6.10	−2.284
sc	2.55	−1.222	2.79	−0.803	∞	0.000	2.81	−2.060
bcc	3.09	−1.382	3.18	−1.264	∞	0.000	3.43	−1.988
fcc	3.86	−1.404	4.04	−1.319	∞	0.000	4.32	−1.965
hcp	2.61,4.98 (2.660, 4.933[a])	−1.449 (−1.325[b])	2.86, 4.63	−1.325	∞,∞	0.000	3.05, 5.99	−1.965
gra	4.26, 4.63	−1.124	4.51, 4.75	−0.720	∞,∞	0.000	4.58, 5.54	−2.092

[a]Experimental data (Ref. 44).
[b]Experimental data (Ref. 42).

TABLE XI. Te lattice structure properties.

	DFT		BOP		SW		Tersoff	
Structure	a,c (Å)	E_c (eV)	a,c (Å)	E_c (eV)	a,c	E_c (eV)	a,c (Å)	E_c (eV)
dc	7.12	−2.272	7.23	−1.943	∞	0.000	6.10	−2.284
sc	3.17	−2.765	3.23	−2.163	∞	0.000	2.81	−2.060
bcc	3.87	−2.551	3.93	−1.941	∞	0.000	2.86	−1.988
fcc	4.84	−2.399	4.95	−1.846	∞	0.000	3.45	−1.965
A8	4.34,6.05 (4.45,5.91)[a]	−2.798 (−2.168)[b]	4.53,5.51	−2.167	∞,∞	0.000	4.97,4.87	−2.060
gra	5.21,6.06	−2.468	5.38,6.63	−1.873	∞,∞	0.000	4.58,5.54	−2.092

[a]Experimental data (Ref. 44).
[b]Experimental data (Ref. 82).

TABLE XII. ZnTe lattice structure properties.

	DFT		BOP		SW		Tersoff	
Structure	a,c (Å)	E_c (eV)	a,c (Å)	E_c (eV)	a,c (Å)	E_c (eV)	a,c (Å)	E_c (eV)
B1	5.67	−2.305	5.59	−2.380	6.14	−0.814	5.62	−2.060
B2	3.57	−1.926	3.48	−1.820	3.67	−2.049	3.43	−1.988
wz	4.25,6.94	−2.387	4.26,6.97	−2.430	4.50,7.69	−1.399	4.32,7.05	−2.284
zb	6.06 (6.101[a])	−2.505 (−2.364[b])	6.03	−2.431	6.36	−2.672	6.10	−2.284
fcs	3.83	−1.876	3.85	−1.924	4.02	−2.675	3.84	−1.831
NiAs			3.91,3.35	−2.263	4.14	−2.617	3.87,3.44	−2.054
$L1_1$			6.85,6.46	−2.380	6.05,9.15	−2.474	5.34,9.97	−1.965
$L1_0$			4.93,3.48	−1.820	4.74,5.61	−0.999	3.84,6.26	−1.831
sc16			7.42	−2.221	8.63	−0.023	7.43	−2.169
Zn_2Te-Ag_2O			6.08	−1.558		Unstable	5.99	−1.770
Te_2Zn-Ag_2O			5.76	−1.712		Unstable	5.99	−1.770
Zn_2Te-ZrO_2			Unstable	Unstable		Unstable	6.83	−1.976
Te_2Zn-ZrO_2			6.48	−1.898		Unstable	6.83	−1.976

[a]Experimental data (Refs. 44 and 47).
[b]Experimental data (Ref. 42).

TABLE XIII. CdZn lattice structure properties.

	DFT		BOP	
Structure	a,c (Å)	E_c (eV)	a,c (Å)	E_c (eV)
B1	5.47	−1.126	5.20	−0.915
B2	3.37	−1.310	3.17	−1.136
wz	Unstable	Unstable	4.29,7.00	−0.626
zb	6.06	−0.740	6.06	−0.626
fcs	3.67	−0.558	3.68	−0.611
NiAs			2.98,4.46	−1.132
$L1_1$			5.14,9.38	−1.181
$L1_0$			4.48,3.16	−1.136
sc16			7.54	−0.622
Cd_2Zn-Ag_2O			6.07	−0.418
Zn_2Cd-Ag_2O			6.05	−0.418
Cd_2Zn-ZrO_2			6.29	−0.935
Zn_2Cd-ZrO_2			Unstable	Unstable

TABLE XIV. Lattice structure properties of three ternary $Cd_{1-x}Zn_xTe$ compounds.

	DFT			BOP		
Structure	a,c (Å)	E_c (eV)	ΔH (eV)	a,c (Å)	E_c (eV)	ΔH (eV)
Cd_3ZnTe_4 sulvanite	6.17	−2.369	0.009	6.26	−2.209	0.030
$CdZnTe_2$ tetragonal $p4m2$	6.38, 4.41	−2.409	0.009	6.38, 4.57	−2.272	0.030
$CdZn_3Te_4$ sulvanite	6.40	−2.452	0.006	6.63	−2.336	0.029

TABLE XV. Elastic constants of ZnTe-zb (GPa).

c_{ij}	Experiment (300 K)[a]	BOP
c_{11}	73.7	77.1
c_{12}	42.3	47.5
c_{44}	32.1	26.5
$c_{44}^{(0)}$		57.1

[(0)]Unrelaxed.
[a]Experimental data (Ref. 46).

TABLE XVI. Intrinsic defect energy E'_D of various defects in ZnTe-zb.

Defect	DFT	BOP	Tersoff[a]
V_{Zn}	2.26	2.65	1.28
V_{Te}	1.98	1.99	1.19
Zn_{Te}	2.57	3.13	−0.10
Te_{Zn}	4.38	2.67	0.10
$Zn_{i,Te}$	2.26	2.41	2.22
$Te_{i,Zn}$	3.52	3.90	2.32
$Zn_{i,Zn}$	1.89	2.28	2.22
$Te_{i,Te}$	4.97	3.85	2.32
$Zn_{i,\langle 110\rangle}$	1.89	2.82	2.05
$Te_{i,\langle 110\rangle}$	3.63	3.94	2.15
$Zn_{i\langle 100\rangle}$	2.98	3.51	1.78
$Te_{i,\langle 100\rangle}$	3.51	3.94	1.87

[a]Literature Tersoff data (Ref. 40).

[1]T. E. Schlesinger, J. E. Toney, H. Yoon, E. Y. Lee, B. A. Brunett, L. Franks, and R. B. James, Mater. Sci. Eng. **32**, 103 (2001).

[2]P. J. Sellin, Nucl. Instrum. Methods Phys. Res., Sect. A **513**, 332 (2003).

[3]A. Peurrung, Mater. Today **11**, 50 (2008).

[4]T. Takahashi and S. Watanabe, IEEE Trans. Nucl. Sci. **48**, 950 (2001).

[5]G. A. Carini, A. E. Bolotnikov, G. S. Camarda, and R. B. James, Nucl. Instrum. Methods Phys. Res., Sect. A **579**, 120 (2007).

[6]U. N. Roy, S. Weiler, J. Stein, A. Hossain, G. G. Camarda, A. E. Bolotnikov, and R. B. James, J. Cryst. Growth **332**, 34 (2011).

[7]V. Babentsov, V. Boiko, G. A. Schepelskii, R. B. James, J. Franc, J. Prochazka, and P. Hlidek, Nucl. Instrum. Methods Phys. Res., Sect. A **633**, S81 (2011).

[8]D. Zeng, W. Jie, T. Wang, G. Zha, and J. Zhang, Nucl. Instrum. Methods Phys. Res., Sect. A **586**, 439 (2008).

[9]C. Szeles, Phys. Status Solidi A **241**, 783 (2004).

[10]C. Szeles, IEEE Trans. Nucl. Sci. **51**, 1242 (2004).

[11]G. Zha, W. Jie, T. Tan, and L. Wang, Phys. Status Solidi A **204**, 2196 (2007).

[12]K. Zweibel, Science **328**, 699 (2010).

[13]X. W. Zhou, D. K. Ward, B. M. Wong, F. P. Doty, J. A. Zimmerman, G. N. Nielson, J. L. Cruz-Campa, V. P. Gupta, J. E. Granata, J. J. Chavez, and D. Zubia, Phys. Rev. B **85**, 245302 (2012).

[14]J. J. Chavez, D. K. Ward, B. M. Wong, F. P. Doty, J. L. Cruz-Campa, G. N. Nielson, V. P. Gupta, D. Zubia, J. McClure, and X. W. Zhou, Phys. Rev. B **85**, 245316 (2012).

[15]D. K. Ward, X. W. Zhou, B. M. Wong, F. P. Doty, and J. A. Zimmerman, J. Chem. Phys. **134**, 244703 (2011).

[16]D. K. Ward, X. W. Zhou, B. M. Wong, F. P. Doty, and J. A. Zimmerman, Phys. Rev. B **85**, 115206 (2012).

[17]D. G. Pettifor, M. W. Finnis, D. Nguyen-Manh, D. A. Murdick, X. W. Zhou, and H. N. G. Wadley, Mater. Sci. Eng. A **365**, 2 (2004).

[18]D. G. Pettifor and I. I. Oleinik, Phys. Rev. Lett. **84**, 4124 (2000).

[19]D. G. Pettifor and I. I. Oleinik, Phys. Rev. B **65**, 172103 (2002).

[20]R. Drautz, D. Nguyen-Manh, D. A. Murdick, X. W. Zhou, H. N. G. Wadley, and D. G. Pettifor, TMS Lett. **1**, 31 (2004).

[21]R. Drautz, D. A. Murdick, D. Nguyen-Manh, X. W. Zhou, H. N. G. Wadley, and D. G. Pettifor, Phys. Rev. B **72**, 144105 (2005).

[22]X. W. Zhou, D. K. Ward, B. M. Wong, and F. P. Doty, Phys. Rev. Lett. **108**, 245503 (2012).

[23]L. Goodwin, A. J. Skinner, and D. G. Pettifor, Europhys. Lett. **9**, 701 (1989).

[24]S. Wolfram, in *The Mathematica Book*, 5th ed. (Wolfram Research, Inc., Champaign, IL, 2004), p. 106ff.

[25]M. R. Hestenes and E. Stiefel, J. Res. National Bureau Stand. **49**, 409 (1952).

[26]D. M. Olsson and L. S. Nelson, Technometrics **17**, 45 (1975).

[27]R. Storn and K. Price, J. Global Optim. **11**, 341 (1997).

[28]S. Kirkpatrick, C. D. Gelatt, and M. P. Vecchi, Science **220**, 671 (1983).

[29]F. H. Stillinger and T. A. Weber, Phys. Rev. B **31**, 5262 (1985).

[30]J. Tersoff, Phys. Rev. B **39**, 5566 (1989).

[31]X. W. Zhou, D. A. Murdick, B. Gillespie, and H. N. G. Wadley, Phys. Rev. B **73**, 045337 (2006).

[32]D. A. Murdick, X. W. Zhou, H. N. G. Wadley, R. Drautz, and D. G. Pettifor, Mater. Res. Soc. Symp. Proc. **859E**, JJ9.7.1 (2005).

[33]J. Oh and C. H. Grein, J. Cryst. Growth **193**, 241 (1998).

[34]M. Nakamura, H. Fujioka, K. Ono, M. Takeuchi, T. Mitsui, and M. Oshima, J. Cryst. Growth **209**, 232 (2000).

[35]Z. Q. Wang, D. Stroud, and A. J. Markworth, Phys. Rev. B **40**, 3129 (1989).

[36]Z. Zhang, A. Chatterjee, C. Grein, A. J. Ciani, and P. W. Chung, J. Electron. Mater. **40**, 109 (2011).

[37]LAMMPS download site: lammps.sandia.gov.

[38]S. Plimpton, J. Comp. Phys. **117**, 1 (1995).

[39]D. S. Borges and J. P. Rino, Phys. Rev. B **72**, 014107 (2005).

[40]M. B. Kanoun, A. E. Merad, H. Aourag, J. Cibert, and G. Merad, Solid State Sci. **5**, 1211 (2003).

[41]M. Czajkowski, R. Bobkowski, and L. Krause, Phys. Rev. A **41**, 277 (1990).

[42]I. Barin, O. Knacke, and O. Kubaschewski, *Thermochemical Properties of Inorganic Compounds* (Springer-Verlag, Berlin, 1977).

[43]M. A. Czajkowski and J. Koperski, Sepctro. Acta A **55**, 2221 (1999).

[44]J. D. H. Donnay and H. M. Ondik, *Crystal Data, Determinative Tables*, 3rd ed., Vol. 2 (inorganic compounds), (US Department of Commerce, National Bureau of Standards, and Joint Committee on Power Diffraction Standards, USA, 1973).

[45]C. Kittel, *Introduction to Solid State Physics*, 7th ed. (Wiley, New York, 1996).
[46]*CRC Handbook of Chemistry and Physics*, 88th ed., edited by D. R. Lide (CRC Press, New York, 2007–2008).
[47]P. Paufler, in *Landolt-Börnstein: Numerical Data and Functional Relationships in Science and Technology. Group III: Crystal and Solid State Physics*, edited by O. Madelung, Vol. 22 (Springer, Berlin, 1987).
[48]S. Grimme, J. Comput. Chem. **27**, 1787 (2006).
[49]B. M. Wong and S. H. Ye, Phys. Rev. B **84**, 075115 (2011).
[50]K. Albe, K. Nordlund, J. Nord, and A. Kuronen, Phys. Rev. B **66**, 035205 (2002).
[51]M. Parrinello and A. Rahman, J. Appl. Phys. **52**, 7182 (1981).
[52]W. A. Harrison, *Electronic Structure and the Properties of Solids* (Freeman, San Francisco, 1980, reprinted by Dover, New York, 1988).
[53]K. Katada, M. Kogachi, and Y. Matsuo, J. Phys. Chem. Solids **34**, 1703 (1973).
[54]B. J. Shaw, Acta Metall. **15**, 1169 (1967).
[55]L. Amirouche and Ş. Erkoç, Int. J. Mod. Phys. C **14**, 905 (2003).
[56]N. Korozlu, K. Colakoglu, and E. Deligoz, J. Phys.: Condens. Matter **21**, 175406 (2009).
[57]B. H. Lee, J. Appl. Phys. **41**, 2984 (1970).
[58]J. R. Morris, C. Z. Wang, K. M. Ho, and C. T. Chan, Phys. Rev. B **49**, 3109 (1994).
[59]*CRC Handbook of Chemistry and Physics*, 90th ed., edited by W. M. Haynes and D. R. Lide (CRC Publications, Internet Version 2012).
[60]L. A. Marqués, L. Pelaz, M. Aboy, and J. Barbolla, Nucl. Instrum. Methods Phys. Res. B **216**, 57 (2004).
[61]C. Z. Wang, C. T. Chan, and K. M. Ho, Phys. Rev. B **42**, 11276 (1990).
[62]L. J. Porter, S. Yip, M. Yamaguchi, H. Kaburaki, and M. Tang, J. Appl. Phys. **81**, 96 (1997).
[63]S. J. Cook and P. Clancy, Phys. Rev. B **47**, 7686 (1993).
[64]M. Ishimaru, K. Yoshida, and T. Motooka, Phys. Rev. B **53**, 7176 (1996).
[65]M. Ishimaru, S. Munetoh, and T. Motooka, Phys. Rev. B **56**, 15133 (1997).
[66]D. A. Murdick, X. W. Zhou, and H. N. G. Wadley, J. Cryst. Growth **286**, 197 (2006).
[67]E. V. Levchenko, A. V. Evteev, I. V. Belova, and G. E. Murch, Acta Mater. **59**, 6412 (2011).
[68]L. A. Zabdyr, J. Electrochem. Soc., **131**, 2157 (1984).
[69]S. B. Zhang and J. E. Northrup, Phys. Rev. Lett. **67**, 2339 (1991).
[70]J. E. Northrup and S. B. Zhang, Phys. Rev. B **47**, 6791 (1993).
[71]G. Zollo and R. M. Nieminen, J. Phys.: Condens. Matter **15**, 843 (2003).
[72]D. J. Chadi, Phys. Rev. B **46**, 9400 (1992).
[73]P. Fernández, J. A. García, A. Remón, J. Piqueras, and V. Muñoz, Semicond. Sci. Technol. **13**, 410 (1998).
[74]V. V. Kosyak, M. M. Kolesnyk, and A. S. Opanasyuk, J. Mater. Sci.: Mater. Electron. **19**, S375 (2008).
[75]G. Tessaro and P. Mascher, J. Cryst. Growth **197**, 581 (1999).
[76]R. D. Feldman, R. F. Austin, P. M. Bridenbaugh, A. M. Johnson, W. M. Simpson, B. A. Wilson, and C. E. Bonner, J. Appl. Phys. **64**, 1191 (1988).
[77]B. Daudin, S. Tatarenko, and D. Brun-LeCunff, Phys. Rev. B **52**, 7822 (1995).
[78]R. Viswanathan, M. S. Baba, D. Darwin Albert Raj, R. Balasubramanian, T. S. Lakshmi Narasimhan, and C. K. Mathews, Spectrochim. Acta, Part B **49**, 243 (1994).
[79]M. Czuchaj, F. Rebentrost, H. Stoll, and H. Presuss, Chem. Phys. Lett. **212**, 534 (1993).
[80]F. Gao, C. Yang, and Y. Dong, Chin. Opt. Lett. **5**, 187 (2007).
[81]K. P. Huber and G. Herzber, *Molecular Spectra and Molecular Structure. IV. Constants for Diatomic Molecules* (Van Nostrand Reinghold, New York, 1979).
[82]I. Barin, *Thermochemical Data of Pure Substances* (VCH, Weinheim, 1993).